International Journal of Pharmaceutics 696 (2026) 126812

Contents lists available at ScienceDirect

International Journal of Pharmaceutics

journal homepage: www.elsevier.com/locate/ijpharm

PEG-β-Cyclodextrin polymer-based formulation to increase the antiangiogenic activity of rutin *in vivo*

Federica De Gaetano [a,*], Eleftheria Dossi [b], Anna Cacciola [a], Noemi Totaro [a], Debora Santonocito [c], Luca Pulvirenti [d], Salvatore Vincenzo Giofrè [a], Giuseppe Paladini [e,*], Alessandro Pilloni [e], Maria Paola Germanò [a], Cinzia Anna Ventura [a]

[a] University of Messina, Department of Chemical, Biological, Pharmaceutical and Environmental Sciences, Viale F. Stagno d'Alcontres 31, 98166 Messina, Italy
[b] Faculty of Engineering and Applied Sciences, Cranfield University, Defence Academy of UK, Shrivenham SN6 8LA, UK
[c] Department of Drug and Health Sciences, University of Catania, 95125, Viale Andrea Doria 6, Catania, Italy
[d] Department of Chemical Sciences, University of Catania, 95125, Viale Andrea Doria 6, Catania, Italy
[e] University of Messina, Department of Mathematics and Computer Sciences, Physical Sciences and Earth Sciences, Viale F. Stagno d'Alcontres 31, 98166 Messina, Italy

ARTICLE INFO

Keywords:
Rutin
β-cyclodextrin polymer
Physical–chemical characterization
In vivo antiangiogenic activity
Zebrafish

ABSTRACT

Rutin (RTN) is a natural flavonoid with well-documented anti-angiogenic, antioxidant, anti-inflammatory, and anti-cancer properties. However, its therapeutic potential is limited by its extremely low water solubility, which results in poor and unpredictable bioavailability. To address these limitations, we developed a new formulation that complexes RTN with a soluble polymeric β-cyclodextrin (βCPCD). βCPCD is synthesized by cross-linking polyethylene glycol (PEG) and β-cyclodextrin (βCD). The high complexing capacity of βCPCD was demonstrated by a ~ 50-fold increase in RTN solubility and complete dissolution within 60 min. These results suggest a dual encapsulation mechanism involving (i) the inclusion of RTN within the βCD cavity and (ii) the allocation of RTN within the free volume of the three-dimensional (3D) polymeric structure. The host–guest interaction was confirmed via UV–Vis titration, NMR, μ-Raman and FTIR-ATR spectroscopy analyses. The thermal stability of the lyophilized complex was assessed by TGA, and the morphology was investigated by SEM. Preliminary docking and molecular dynamics simulations were carried out considering a local scenario consisting of a single RTN and a βCD-PEG unit. The excellent biocompatibility of βCPCD in Danio rerio zebrafish embryos (survivability > 95%) and the notable enhancement of the antiangiogenic effect of the RTN complex compared to the free drug highlight the potential of βCPCD as an effective delivery system to improve RTN performance.

1. Introduction

Angiogenesis is a complex physiological process by which new capillaries develop from pre-existing arteries. This process is supported by the coordinated interactions of multiple cell types and mediators (Kerbel and Folkman, 2002).

It plays a critical role in various pathological conditions, such as in cancer progression (Nishida et al., 2006; Papetti and Herman, 2002). Muthukkaruppan et al. (Muthukkaruppan et al., 1982) observed that, in the absence of blood circulation, cancer cells injected into different regions of the same organ grew to 1–2 mm^3 before stopping, whereas they grew beyond a diameter beyond 2 mm^3 in area in which angiogenesis was induced. These findings highlight the essential role of neovascularization in facilitating tumor growth.

Anti-angiogenesis treatment involves using of bioactive molecules (De Gaetano et al., 2023; Najmi et al., 2022), that cooperate to reduce morbidity and mortality rates associated with carcinomas (Al-Ostoot et al., 2021).

Plants, fruits, and other natural products are an important source of bioactive compounds and have recently received significant attention in pharmaceutical, nutraceutical, and cosmeceutical fields due to their exceptional properties and advantages, such as biocompatibility and low toxicity (Narayanankutty et al., 2024). In this context, flavonoids have emerged as key natural bioactive compounds (Cacciola et al., 2025;

* Corresponding authors.
E-mail addresses: fedegaetano@unime.it (F.D. Gaetano), e.dossi@cranfield.ac.uk (E. Dossi), anna.cacciola1@studenti.unime.it (A. Cacciola), noemi.totaro@studenti.unime.it (N. Totaro), debora.santonocito@unict.it (D. Santonocito), luca.pulvirenti@unict.it (L. Pulvirenti), gpaladini@unime.it (G. Paladini), alepilloni@unime.it (A. Pilloni), mariapaola.germano@unime.it (M.P. Germanò), caventura@unime.it (C.A. Ventura).

https://doi.org/10.1016/j.ijpharm.2026.126812
Received 14 November 2025; Received in revised form 13 March 2026; Accepted 22 March 2026
Available online 27 March 2026
0378-5173/© 2026 The Author(s). Published by Elsevier B.V. This is an open access article under the CC BY license (http://creativecommons.org/licenses/by/4.0/).

Zheng et al., 2025) due to their strong antiangiogenic activity (De Gaetano et al., 2023). Among them, rutin (RTN), a naturally occurring flavonol(Fig. 1) (Al-Dhabi et al., 2015) has been investigated for treating various chronic diseases, including cancer (Pandey et al., 2021; Pravin et al., 2024), diabetes (Ghorbani, 2017), hypertension (Bazyar et al., 2023), hypercholesterolemia (Liang et al., 2021; Ziaee et al., 2009), bacterial infections(De Gaetano et al., 2024c), and, oxidative stress (Sharma et al., 2013a) as well as its potential role in angiogenesis-dependent diseases (Guruvayoorappan and Kuttan, 2007).

Treatment with RTN was shown to significantly reduce the number of tumor-directed capillaries induced by injecting B16F-10 melanoma cells into the ventral side of C57BL/6 mice, achieving a 43.35% inhibition rate. RTN was also found to inhibit the proliferation, migration, and capillary formation abilities of human endothelial cells in vitro. Similar results were obtained by Alonso-Castro et al. (Alonso-Castro et al., 2013) in nude mice bearing SW480 colon cancer tumors. These results showed an increase in mean survival time of 50 days and a 55% reduction in serum VEGF levels compared to untreated mice.

While these results demonstrate the potential of RTN in cancer treatment, its clinical development remains challenging due to its very low water solubility (0.125 mg/mL) (De Gaetano et al., 2024c; Liu et al., 2020), which reduces its absorption, making bioavailability low and unpredictable (Bhuvaneswari and Kumudha, 2024; Serri et al., 2024).

Numerous carriers have been developed to improve solubility, stability and biological activity of RTN in various health disorders (Bansal et al., 2025; Sharma et al., 2013b). These carriers include native and modified β-cyclodextrin (βCD) inclusion complexes (Chang et al., 2023; Corina et al., 2017; Liu et al., 2022; Ming Liu et al., 2024; Pham et al., 2024; Zhou et al., 2012); solid dispersions (Nguyen et al., 2025), lipid-based nanocarriers (Chen et al., 2022; Cristiano et al., 2021; De Gaetano et al., 2021; Li et al., 2023); nanosponges (Chauhan and Malviya, 2023; Sri et al., 2018); polymeric particles (Rashidinejad et al., 2024) and hybrid systems obtained by combination of CDs and liposomes (Sguizzato et al., 2025) or by incorporating CDs into hydrogels (Naeem et al., 2023).

Of these, CDs are the most widely studied carrier for RTN due to their structural properties and strong host–guest affinity toward various lipophilic substances (De Gaetano et al., 2024a, 2024b; Esteso and Romero, 2024; Paladini et al., 2025). Especially β- and γCD offer excellent encapsulation capabilities for small molecules (De Gaetano et al., 2022; Loftsson et al., 2019; Saokham et al., 2018) and can undergo chemical functionalization to enhance, solubility, reduce toxicity in biological environment (De Gaetano et al., 2025; Kali et al., 2024) and obtain sustained drug release (Pedotti et al., 2015). βCD, the most extensively studied, can be grafted onto polymers as a side group (Sirin et al., 2022; Wang et al., 2019), used to create star-shaped systems (Rojas-Aguirre et al., 2019), and incorporated into a polymer chains to form polyrotaxanes (Kali et al., 2024; Puig-Rigall et al., 2019), can be cross-linked with various chemistries, such as epichlorohydrin (El-Remaily and Soliman, 2016; Morin-Crini et al., 2018), diisocyanates (Gubitosa et al., 2025; Xie et al., 2016), diglycidyl ethers (Luppi et al., 2019), carbonyl compounds (Trotta et al., 2012b) and other cross-linkers (Concheiro and Alvarez-Lorenzo, 2013) to produce three-dimensional (3D) porous polymer network (Feng et al., 2021; Goyal et al., 2023; Y. Liu et al., 2021; Liu et al., 2018; Mallard et al., 2020).

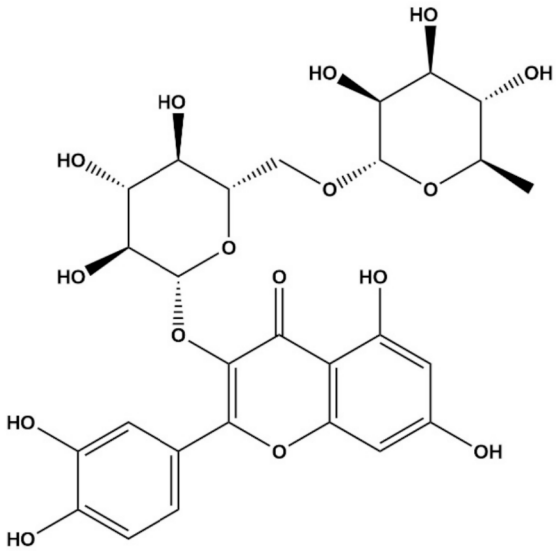


Fig. 1. Molecular structure of RTN.

Among cross-linked polymers, the supramolecular network formed by βCD and PEG has received significant attention for drug delivery due to the excellent water solubility, non-toxicity, high biocompatibility, and prolonged circulation time of PEG (Raina et al., 2021). Unlike linear or star-shaped PEGylated βCD polymers, in which CD remains a discrete, non-crosslinked molecular unit with independent host–guest sites, cross-linked PEGylated-CDs polymers form an integrated network in which both the macrocycle and PEG chains contribute to the polymeric architecture. This offers advantages beyond increased solubility, including improved loading capacity and diffusion-controlled release, compared to monomeric CDs.

Supramolecular structures obtained by cross-linked βCD with PEG-diglycidyl ethers (Rodriguez-Tenreiro et al., 2006) form hydrogels and offer a good combination of βCD and PEG properties for use in biological systems. An alternative cross-linked βCD-PEG polymer (βCPCD), soluble in water and alcohols, was reported by Luppi et al. (Luppi et al., 2019). This polymer significantly enhances the water solubility of curcumin and improves its permeability across Caco-2 cell monolayers (Haimhoffer et al., 2021). The cross-linked network is characterized by a high hydrodynamic/free volume and non-occupied spaces within the molecular matrix. This enhances drug loading by including in the CDs cavity and allocating in the free volume confined by the 3D polymeric network (Shurshina et al., 2021; Tsai and Chiu, 2022). βCPCD has also demonstrated excellent biocompatibility, highlighting its potential as an effective drug delivery platform (Haimhoffer et al., 2021).

To the best of our knowledge, no studies concerning the use of linear and cross-linked βCD polymers to improve the biological performance of RTN have been published.

Due to the potential advantages that such a carrier could offer RTN delivery in terms of solubility, stability, and bioactivity, this work reports, for the first time, a supramolecular RTN/βCPCD system that enhances the antiangiogenic potential of RTN for cancer treatment. The new complex was characterized though UV–Vis spectroscopy, NMR, μ-Raman, Fourier transform infrared spectroscopy in attenuated total reflectance geometry (FTIR-ATR), thermogravimetric analysis (TGA) and morphological evaluation. Preliminary docking and molecular dynamics (MD) simulations of the RTN/βCD-PEG unit were performed, and the biocompatibility and antiangiogenic effects of the RTN/βCPCD formulation were tested *in vivo* using zebrafish (Danio rerio) embryos.

2. Materials and methods

2.1. Materials

Rutin (RTN, MW 610.53 g/mol, 3,3′,4′,5,7-pentahydroxyflavone-3-rhamnoglucoside, chemical formula $C_{27}H_{30}O_{16}$) β-ciclodesxtrin (β-CD, chemical formula $C_{42}H_{70}O_{35}$, MW 1134.98 g/mol, purity ≥ 97%), polyethylene glycol diglycidyl ether (PEGDGE, MW 500 Da, polydispersity index = 1.7), 2-Methoxyestradiol (chemical formula $C_{19}H_{26}O_3$), dimethyl sulfoxide (DMSO), nitro blue tetrazolium (NBT), 5-bromo-4-chloro-3-indolyl phosphate (BCIP), 1-phenyl-2-thiourea (PTU), phosphate buffered saline (Tablets, High-Purity), Tris buffered saline, sodium chloride (NaCl, purity ≥ 99.0%), magnesium chloride hexahydrate (MgCl), Tween® 20, were purchased from Sigma-Aldrich

Chemie® (St. Louis, MO, USA). βCPCD (MW of monomeric unit 2500 Da) was kindly provided by the Centre for Defence Engineering and Physical Sciences, Cranfield University (Shrivenham, United Kingdom). Deuterated solvents used for NMR analyses, methanol (purity ≥ 99.8%), ethanol (purity ≥ 99.9%, GC) and chemicals and reagents of analytical grade were supplied by Merck® (Darmstadt, Germany). Dialysis bags were Spectra/Por® 18 × 11.5 mm Dialyse-Membrane (MWCO: 3500, Spectrum Laboratories, Inc., Rancho Dominguez, CA, USA). Double-distilled water used throughout study was filtered through 0.22 μm Millipore®.

2.2. Preparation of the RTN/βCPCD inclusion complex and physical mixture

The RTN/βCPCD inclusion complex was prepared by freeze-drying method. First, the polymer (0.5%, m/v) was dissolved in 10 mL of water. Then, solid RTN (6 mg) was added to the aqueous solution. The suspension was mechanically stirred (500 rpm) in the dark at room temperature for one week until equilibrium was reached.

The suspension was then filtered (Sartorius Minisart-SRP 15-PTFE filters, 0.22 μm, Bedford, MA, USA), to eliminate undissolved RTN, and this solution was frozen and freeze-dried for 72 h using a Christ Alpha 2–4 LSC basic freeze-dryer (Martin Christ Gefriertrocknungsanlagen GmbH, Osterode am Harz, Germany) to obtain the powdered RTN/βCPCD complex.

The complex was also prepared by freeze-drying a hydroalcoholic solution containing the polymer and RTN. In brief, RTN (6 mg) was dissolved in 1 mL of methanol and added dropwise to a 9 mL aqueous solution containing 0.5% (m/v) βCPCD. The final hydroalcoholic solution was kept under continuous magnetic stirring at 500 rpm for 5 h, then filtered, to eliminate any undissolved particles, frozen and freeze-dried for 72 h using the previously described apparatus to obtain the powdered RTN/βCPCD complex.

Both procedures were performed away from direct light.

The obtained solid samples were stored in a desiccator at room temperature until further analysis.

The RTN/βCPCD physical mixture was prepared by accurately weighing RTN (6 mg) and βCPCD (50 mg), then blending them manually using a mortar and pestle to ensure homogeneous distribution.

2.3. Preparation of RTN/βCD inclusion complex and RTN/PEG solid dispersion

The RTN/βCD inclusion complex was prepared using freeze-drying method. Briefly, 6 mg of RTN was solubilized in 1 mL of methanol and added to an aqueous solution (9 mL) containing 0.5% (m/v) βCD. The solution was magnetically stirred in the dark, at room temperature, for 5 h, then frozen and freeze-dried, using the same apparatus and condition described in the 2.2 section.

RTN/PEG solid dispersion was obtained by solubilizing PEG (0.5%, m/v) in 9 mL of water, then RTN (6 mg) solubilized in 1 mL of methanol was added. The solution was mechanically stirred in the dark, at room temperature, for 5 h, then it was freeze-dried.

All the solid samples were stored in a desiccator at room temperature until water solubility was determined.

2.4. Determination of encapsulation parameters of RTN/βCPCD complexes

Encapsulation efficiency (E.E.%) and drug loading (D.C.%) of the RTN/βCPCD complexes were determined by direct method. Specifically, the freeze-dried complexes were weighted and solubilized in methanol/water mixture (80/20, v/v). The samples opportunely diluted were analyzed by UV–Vis spectroscopy (Shimadzu double-beam spectrophotometer, model UV-1800, Kyoto, Japan) to quantify RTN. The maximum absorption wavelength (λ_{max}) of 352 nm was used. A calibration curve of RTN was constructed in methanol/water mixture (80/20, v/v) over a concentration range of 0.001 to 0.05 mg/mL yielding a linear regression coefficient (R^2) of 0.9994.

E.E.% and D.C.% were then determined using the following equations (Eq (1), Eq (2):

$$E.E(\%) = \frac{\mathrm{RTN}_{\mathrm{encapsulated}}}{\mathrm{RTN}_{\mathrm{initially\ added}}} \times 100 \quad (1)$$

$$D.E(\%) = \frac{RTN_{encapsulated}}{\mathrm{Weight\ of\ complex}} \times 100 \quad (2)$$

2.5. Water solubility evaluation

The solubility of RTN/βCPCD complex was evaluated in comparison to RTN/βCD inclusion complex and RTN/PEG solid dispersion. Excess amount (1 g) of each sample was dispersed in 10 mL of water. The suspensions were maintained in the dark at a controlled temperature (25.0 ± 0.5 °C) and magnetically stirred at 100 rpm. At predetermined time intervals, 1 mL aliquot of the suspensions were taken, filtered through Sartorius Minisart-SRP 15-PTFE filters (0.22 μm, Bedford, MA, USA), and the solutions, opportunely diluted with methanol and water to have a final methanol/water mixture of 80:20 (v/v), were analyzed by UV–Vis spectroscopy to quantify RTN, by using the same apparatus and conditions previously described (see 2.4 paragraph). After each sampling, the volume of the suspensions was restored to 10 mL by adding water to maintain a constant volume throughout the experiment. Analyses were conducted until a constant value of RTN in the solution was obtained. The assay was performed in triplicate, and the data was corrected for dilution.

2.6. Dissolution profile

Dissolution studies were performed according to the guidelines outlined in the 44th edition of the United States Pharmacopeia (USP). In brief, free RTN (35 mg) or an equivalent amount of RTN in the complex or physical mixture was dispersed into 900 mL of water. The dissolution medium was kept in the dark at 37.0 ± 0.5 °C with continuous magnetic stirring at 100 rpm. At predetermined time (0, 3, 5, 10, 15, 30, 45, 60, 120, and 180 min), 1 mL aliquots of the dissolution medium was collected and immediately filtered to remove undissolved particles. The filtered samples were then appropriately diluted with methanol and water, then analyzed using UV–Vis at λ_{max} of 352 nm to determine the concentration of dissolved RTN. After each sampling, the suspension volume was adjusted back to 900 mL by adding preheated water (37.0 ± 0.5 °C) to maintain a constant volume throughout the experiment. The assay was conducted in triplicate, and the data were corrected for dilution.

2.7. Evaluation of drug release from RTN/βCPCD complex

The release of RTN from the complex was evaluated using a dialysis method, employing synthetic cellulose membranes with a molecular weight cutoff (MWCO) of 3.5 kDa, previously hydrated for 24 h. Dialysis tubes were filled with 1 mL of the RTN/βCPCD complex dispersion (containing 1 mg of RTN) or with an equivalent amount of free RTN, solubilized in DMSO and subsequently diluted in pH 7.4 buffer (final DMSO concentration 0.2% v/v), which also served as the dialysis medium. The tubes were incubated under continuous agitation (150 rpm) at 37 ± 1 °C in a thermostatic bath (Telesystem 15.40, Thermo Scientific, Waltham, MA, USA) equipped with a temperature control unit (Telemodul 40C, Thermo Scientific, Waltham, MA, USA). At predetermined time intervals (0.5, 1, 5, 7, 24, 48, 72, and 120 h), the dialysis medium was completely refreshed with fresh pH 7.4 buffer.

The amount of RTN released was quantified by UV–Vis spectroscopy through direct analysis of the collected medium. For data interpretation,

a calibration curve of RTN was constructed in a methanol/PBS mixture (80/20, v/v), over the concentration range 0.001–0.05 mg/mL, yielding a linear regression coefficient ($R^2 = 0.9997$).

2.8. Phase-solubility studies

An excess amount of solid RTN, exceeding its intrinsic solubility, was added to aqueous solutions with increasing concentrations of βCPCD (0–10 mg/mL). The suspensions were kept in the dark and stirring continuously at 25.0 ± 0.5 °C for 1 week to reach equilibrium. Post-incubation, the suspensions were filtered and diluted in methanol to have a final methanol/water mixture (80:20, v/v). The RTN concentration in each solution was determined using UV–Vis spectrophotometry at 352 nm. The experiments were carried out in triplicate.

2.9. Uv–vis titration studies

A stock solution of free RTN (0.04 mM) was prepared in methanol and divided into separate vials (1 mL), whilst solutions containing increasing concentrations of βCPCD (0–1% m/v) were prepared in water. 4 mL of each prepared βCPCD solution were added to the vials containing RTN solution and mechanically stirred at 500 rpm for 5 h, under light-protected conditions. The samples were then analyzed via UV–Vis spectroscopy in the wavelength range of 200–800 nm.

2.10. Nuclear magnetic resonance (^{1}H NMR) measurements

Samples with equivalent concentrations (15 mM) of RTN and RTN/βCPCD inclusion complex were prepared in a D_2O/CD_3OD (80:20, v/v) solution and transferred to 5-mm NMR tubes for spectrum acquisition. All spectra were recorded at 9300 K for 64 scans using a Varian Unity Inova 500 MHz (11.75 T) spectrometer. D_2O (4.79 ppm) was used as an internal reference.

2.11. Aggregation studies

The self-aggregation of βCPCD alone or complexed with RTN in aqueous solution was assessed using a Zetasizer PRO – Blue Label instrument (Malvern Panalytical, UK), operated with ZS XPLORER software version 3.3 (PSS0048-20). Measurements were conducted over a βCPCD concentration range from 0.01 to 2.5% (m/v), considering that the lowest detectable concentration by the instrument was 0.01% (m/v).

Particle size was measured using Dynamic Light Scattering (DLS), at scattering angles of 12.8° and 173°, employing Non-Invasive Back Scattering (NIBS) technology. Zeta potential was determined via Electrophoretic Light Scattering (ELS), using the M3-PALS (Phase Analysis Light Scattering) technique in Constant Current Mode, ensuring high precision in the evaluation of electrophoretic mobility.

All freeze-dried samples were poured in deionized water, magnetically stirred at 500 rpm, for 0.5 h and analyzed at controlled temperature (25 ± 0.1 °C).

To assay physical stability of the formulations, all samples were maintained in the dark, at controlled temperature (25 ± 0.1 °C) for 1 month. Then, sizes and zeta potential values were determined.

2.12. Thermal gravimetric analysis (TGA)

Thermogravimetric analysis (TGA) was carried out using a Discovery SDT 650 instrument (TA Instruments-Waters LLC, Milford, MA, USA). Measurements were taken over a temperature range of 25–800 °C under a controlled nitrogen atmosphere (100.0 mL/min) to prevent oxidative degradation, with a constant heating rate of 20 °C/min. Specifically, weighed samples (5–10 mg) of free RTN, βCPCD alone, RTN/βCPCD complex, and RTN/βCPCD physical mixture were placed in alumina crucibles and analyzed in triplicate to ensure reproducible data.

2.13. Scanning electron microscopy (SEM)

SEM analyses were performed by using a field emission scanning electron microscope (FESEM) ZEISS VP 55 beam-accelerating voltage of 5 kV. SEM images were analysed by using ImageJ software to improve the brightness and contrast.

2.14. μ-Raman measurements

μ-Raman measurements were carried out on free RTN, βCPCD alone, RTN/βCPCD complex and physical mixture as previously prepared, through a portable Raman "BTR 111 Mini-Ram TM" (B&W Tek, Inc., Newark, NJ, USA) spectrometer. The instrument is supplied with a 785 nm diode laser source and a thermoelectrically cooled CCD detector, with a 280-mW maximum laser power at the excitation port. Spectra were registered in the 500 − 1800 cm^{-1} with a resolution of 8 cm^{-1} and an acquisition time of 40 s × 16 scans. The instrument was calibrated by using the silicon chip peak at 520.6 cm^{-1}, which guaranteed the optimal instrument performance. The system includes a BAC151B Raman microscope, mounting an 80 × objective with a working distance of ~ 1.25 mm and a laser beam spot size of ~ 25 μm. The laser maximum power delivered to the samples was ~ 40 mW.

2.15. FTIR-ATR measurements

FTIR-ATR spectra were collected using a Bomem DA8 Fourier transform spectrometer (BOMEM, Saint Laurent, QC, Canada), equipped with a Globar source, a KBr beamsplitter, and a thermoelectrically cooled deuterated triglycine sulphate (DTGS) detector. Measurements were performed in the 400 – 4000 cm^{-1} wavenumber range, with a spectral resolution of 4 cm^{-1}. For each run, 100 consecutive scans were averaged in order to ensure a satisfactory signal-to-noise ratio and high reproducibility. Samples were placed in direct contact with the surface of a single-reflectance ATR accessory (Golden Gate, fitted with a diamond crystal). The obtained FTIR spectra were appropriately normalized to account for the effective number of absorbing species. No smoothing procedure was applied; baseline correction and normalization were carried out using the Spectracal software package GRAMS (Galactic Industries, Salem, NH, USA).

2.16. Molecular docking

Docking simulations were carried out considering a local scenario consisting of a single RTN and βCD-PEG unity (βCPCDm) using the *Maestro* modelling suite of the *Schrödinger* software (Schrödinger Inc.). First, the 3D structure of RTN (ligand) was recovered from *PubChem* (CID: 5280805) and structurally optimized through the *Ligprep* sub-tool by setting the OPLS4 as force field and the *Epik* option to generate all relevant molecular states at a pH ~ 7.4. Concerning βCPCDm (receptor), a high-resolution native βCD was obtained from *PubChem* (CID: 444041), and manually functionalized through the addition of a single PEG chain attached to a primary hydroxyl group of a βCD glucose unit *via* a covalent ether bond, using the *Maestro Builder* module. The geometry of the resulting βCPCDm was then optimized taking advantage of the 5000-steps of Polak-Ribiere conjugate gradient (PRCG) energy minimization method of the *MacroModel's Macrocycle Conformational Sampling* (MCS) tool (Schrödinger Inc.). The optimized structure was used to generate a docking grid of 37 Å × 37 Å × 37 Å by assuming the entire βCPCDm as active site. The *Glide* module was used to formally compute all possible docking poses, at T = 300 K and pH = 7.0 ± 2.0, according to the extra precision' (XP) flexible docking method, based on the assessment of the minimum coupling energy.

Each generated docking XP pose of the RTN/βCPCDm inclusion complex was then subjected to the *Molecular Mechanics Generalized Born Surface Area* (MM-GBSA) method for the quantification of the binding affinity (ΔG_{bind}).

2.17. Molecular dynamics (MD) simulations

The docked ligand pose with the optimal Glide score (lowest binding energy) was utilized as starting point for molecular dynamics (MD) simulations. The structures of both RTN and βCPCDm were exported as PDB files and their topology were retrieved from Automated Topology Builder (ATB) and the Repository 3.0 available on-line (Adeoye et al., 2020; Stroet et al., 2018). MD simulations were performed in the NPT ensemble through the GROMACS 2025.3 (Abraham et al., 2015) wizard extension implemented in the SAMSON platform (2025-R3, OneAngstrom), using the GROMOS-96 54a7 force field (Oostenbrink et al., 2004; Poger et al., 2010; Poger and Mark, 2010; Schmid et al., 2011). The inclusion complex was solvated in a water cubic box consisting of 4305 water molecules modeled using the simple point charge (SPC) parametrization (Berendsen et al., 1981). The steepest descent algorithm was applied to minimize the energy of inclusion complex by acting on unreasonable stereo-chemical conflicts and atomic contacts, as well as to relax the water molecules surrounding the system, by performing 50.000 steps for this process. After an initial positional restraint to the ligand, the system was equilibrated under both NVT (at 300 K) and NPT (at 300 K and 1 bar) conditions for 1 ns. Subsequently, production MD simulations were performed for 40 ns using the equilibrated atomic coordinates as starting configuration, with a time step for the integration of the equation of motion set to 2 fs. All the bond lengths were restricted by using the LINear Constraint Solver (LINCS) algorithm (Hess et al., 1997). The temperature was set at 300 K using the velocity-rescaling coupling method (Baumketner, 2009; Bussi et al., 2007; Mojdehi et al., 2021) with a time constant of 1 ps, while pressure was maintained at 1 bar using the C-rescale barostat with a coupling time constant of 5 ps and an isothermal compressibility of 4.5×10^{-5} bar^{-1}. MD-related outputs, including snapshot analysis, root mean square deviation (RMSD) and radius of gyration (Rg), were assessed for the receptor and ligand in order to evaluate conformational stability.

2.18. Maintenance, breeding, collection, and exposure of zebrafish embryos

Adult male and female zebrafish (*Danio rerio*, wild-type AB strain) were maintained in continuous-flow aquaria at 28.5 ± 0.5 °C under a 14/10-hour light/dark photoperiod, following standard protocols (Westerfield, 2000). The zebrafish were fed live brine shrimp (*Artemia salina*) three times daily. The eggs obtained from natural spawning were collected and examined under a stereomicroscope, to exclude damaged or unfertilized eggs. Additionally, embryos exhibiting normal cleavage and developmental synchronization were selected to ensure experimental homogeneity. For the studies, embryos at 24 h post fertilization (hpf) were manually dechorionated, randomly transferred into 96-well microplates (one embryo per well) and exposed to increasing concentration of free and complexed RTN (0.01–1 mg/mL). βCPCD alone was assayed at a broader range concentration respect to the amount contained in the complex (0.05–50 mg/mL). Free RTN was solubilized in 0.2% (v/v) DMSO and opportunely diluted with embryo medium. The complex and the free polymer were solubilized directly in embryo medium without the use of DMSO. Embryos exposed to DMSO (0.2%) were used as a negative control group. The sample size was set at n = 20 embryos per group, replicated in independent experiments (N = 3 to 6), determined to be sufficient for statistical power based on previous laboratory data. Embryos exposed to different treatments were observed after 48 h to record developmental abnormalities or mortality. To minimize observer bias, the morphological assessment and outcome measurements were performed by an investigator blinded to the treatment allocation. All procedures involved zebrafish embryos < 120 hpf and were therefore not subject to animal experimentation regulations according to the European Directive 2010/63/EU.

All the experiments were conducted in compliance with the ethical guidelines outlined in the *National Institutes of Health Guide for the Care and Use of Laboratory Animals*.

2.19. Antiangiogenic activity: quantitative determination of endogenous alkaline phosphatase (EAP) activity

For the evaluation of the antiangiogenic activity, the endogenous alkaline phosphatase (EAP) activity was quantified as a marker of vessel growth in control and treated embryos (Iannuzzi et al., 2019). Zebrafish embryos at 24 hpf (n = 20) were incubated at 28.5 °C with the compounds at the concentrations indicated in the 2.18 section. Embryos exposed to DMSO (0.2%) were used as a negative control group. (2)-Methoxyestradiol (0.006 mg/mL) was employed as positive control.

At 72 hpf, zebrafish embryos were sequentially dehydrated using increasing concentrations of methanol, rinsed three times with a diethanolamine buffer (1 M, pH 9.8), and subsequently incubated with p-nitrophenyl phosphate disodium salt (0.5 mg/mL) for 30 min at room temperature. The enzymatic reaction was terminated by adding 2 M NaOH. The optical density (OD) of the end product was measured at 405 nm using a microplate reader (AMR-100, Allsheng).

The extent of vascular growth was quantified as the percentage of OD relative to the untreated control and expressed as the percentage of inhibition, according to Equation (3) Eq. (3):

$$Inhibition(\%) = \frac{OD_{control} - OD_{treated}}{OD_{control}} \times 100 \quad (3)$$

2.20. Antiangiogenic activity: the alkaline phosphatase (ALP) staining assay

The alkaline phosphatase (ALP) staining assay was performed using the nitro blue tetrazolium (NBT, Sigma) and 5-bromo-4-chloro-3-indolyl phosphate (BCIP, Sigma) substrates following the modified method of Wang et al., 2007 (Wang et al., 2007). At 24 hpf, before sample administration (free and complexed RTN), all the embryos were treated with PTU (final concentration 0.2 mM) to prevent pigmentation and facilitate blood vessel observation. 2-Methoxyestradiol was used as positive control, while embryos exposed to 0.2% DMSO served as the negative control group. At 72 hpf embryos were fixed with 4% paraformaldehyde in PBST (phosphate-buffered saline + 0.1% tween-20) for 30 min. Then, the embryos were dehydrated with ethanol, rinsed with PBST and equilibrated with NTMT (Tris buffer 100 mM pH 9.5; NaCl 100 mM; MgCl 2 50 mM; Tween-20 0.1%), The staining reaction was started incubating embryos with a NBT/BCIP solution for about 15–30 min according to the protocol described for the NBT/BCIP ready-to-use tablets. After the staining reaction was completed, the embryos were washed with PBST. The images of the lateral view of the embryos were captured using a stereomicroscope (SMZ-171 Series, Motic) equipped with a digital camera (Moticam® 5 plus). The total length, number and area of intersegmental vessel (ISV) were measured using Motic Images Plus 3.1 software. Results were expressed as percentage of inhibition (%) of the treated groups compared to negative control group (100% of activity) and are presented as mean values ± standard deviation (SD). For the test, at least 20 embryos for each concentration were used.

2.21. Statistical analysis

Statistical analysis was performed using GraphPad Prism 6 (GraphPad Software Inc., San Diego, CA, USA). Data are expressed as mean ± SD from three independent experiments. Differences between groups were assessed using one–way ANOVA followed by Bonferroni's post hoc test for multiple comparisons, or Dunnett's post hoc test for comparisons versus the control group (RTN). A p–value < 0.001 was considered statistically significant, while extremely significant differences were reported as p < 0.0001".

3. Results and discussions

RTN has a very low water solubility (0.125 mg/mL (De Gaetano et al., 2024c; Liu et al., 2020), resulting in low and erratic oral bioavailability. To enhance its solubility and promote biological activity, RTN was complexed with a "two-in-one" β-CD-PEG cross-linked and water-soluble polymer (βCPCD), which was previously synthesised by Luppi et al. (Luppi et al., 2018). The complex was prepared by lyophilising a solution containing RTN and βCPCD. First, the polymer solubilised in water and the RTN was added as solid powder. After prolonged mechanical stirring (1 week), the suspension was filtered to remove the insoluble drug and then lyophilized to obtain a powder sample with moderate RTN loading (32% E.E. and 0.61% D.C.). To improve the encapsulation parameters, RTN was solubilized in methanol and this solution was added to aqueous solution containing the polymer. This hydroalcoholic solution was then mechanically stirred for 5 h and lyophilized to produce a fluffy, slightly yellow powder with an 100% E. E. and 11% D.C. The addition of a small amount of methanol kept the RTN in solution throughout the preparation process, preventing precipitation and facilitating molecular encapsulation (Liu et al., 2022; Savic et al., 2016). Due to the high E.E., only the latter complex was subjected to deeper chemical and physical characterization in both in aqueous solution and in the solid state.

3.1. In-solution studies

We evaluated the effect of complexation with βCPCD on the aqueous solubility of RTN, comparing it with the RTN/βCD inclusion complex and RTN formulated as a solid dispersion with PEG 500. The RTN/βCPCD complex showed an approximately 50-fold increase, RTN/βCPCD complex a 5-fold increase, and RTN/PEG solid dispersion a 1.8-fold increase.

The superior solubilizing effect of βCPCD clearly demonstrates the importance of its architecture, enabling more efficient drug-carrier interactions than βCD or PEG are used individually.

Unlike native βCD, βCPCD provides a 3D cross-linked network in which βCD cavities are interconnected through PEG chains (Luppi et al., 2018; Trotta et al., 2012c; Utzeri et al., 2022; Wehl et al., 2025). This structure generates a heterogeneous microenvironment characterised by hydrophobic nanodomains (i.e. the cavity of the CD), interconnected channels, and free volume within the polymeric matrix. These features are absent in monomeric βCD (Wehl et al., 2025).

On the other hand, PEG primarily acts as a hydrophilic carrier, promoting drug solubility through by improving wettability (Christoforou et al., 2025). Thus, multiple concurrent interactions could contribute to RTN solubilization in βCPCD: (i) the inclusion of the RTN's hydrophobic moieties within the βCD cavities via host–guest complexation; (ii) the formation of hydrogen bonds between the hydroxyl groups of RTN and the hydroxyl functionalities of the βCD-PEG of the polymer network; and (iii) the RTN's physical entrapment within the interstitial spaces of the crosslinked structure, as reported for βCD-based nanosponges (Trotta et al., 2012b). These mechanisms all contribute to an increase in E.E. and apparent solubility (Harada et al., 2009).

The formation of a complex between RTN and βCPCD significantly affected the dissolution rate of the drug. Fig. 2 shows the comparative dissolution profiles of the RTN/βCPCD complex, the free RTN and the corresponding physical mixture. The complex exhibited 45.6% (w/w) dissolution within the first 5 min, achieving complete dissolution within 60 min. By contrast, free RTN dissolved by only 10% (w/w) over the same time interval, whereas the physical mixture achieved 23.66% (w/w). Several factors can contribute to the fast dissolution rate of complexed RTN. Specifically, i) complexation with βCPCD improves the apparent aqueous solubility of RTN, thus preventing precipitation on the drug, ii) the freeze-drying process reduces the crystallinity of RTN, producing a porous amorphous solid with increased surface area; iii) the high hydrophilicity of βCPCD enhances the wettability of RTN, facilitating its solubilization.

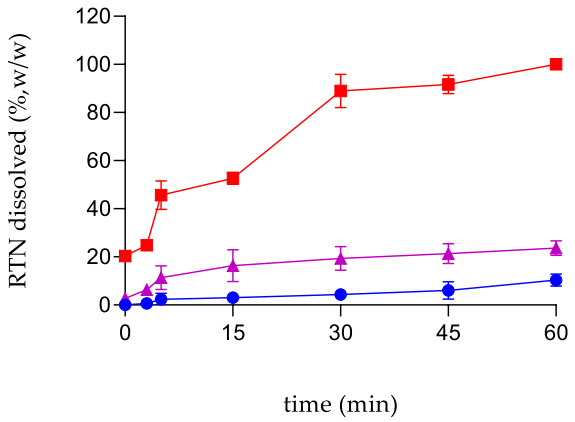


Fig. 2. Dissolution profiles of free RTN (circles, blue line), the physical mixture (triangles, purple line), and the inclusion complex (squares, red line) in water at 25 ± 0.5 °C. Results are expressed as mean ± SD from three independent experiments. Error bars, when not visible, fall within the symbols. Dissolution data for the inclusion complex were significantly significant compared to free RTN according to one–way ANOVA followed by Bonferroni's post hoc test (***$p < 0.001$).

A moderate increase in the dissolution rate compared to the free RTN was also observed for the physical mixture. This improvement can be attributed to the *in situ* formation of the complex at the solid–liquid interface following the fast βCPCD solubilization (Li et al., 2011). However, this process is slow and incomplete because it only occurs upon the solid contacting the solvent, depending on molecular diffusion. This results in a marginal enhancement of RTN dissolution.

This behavior demonstrated the superior efficiency of RTN/βCPCD complex compared to the physical mixture, confirming its role in substantially and immediately enhancing RTN dissolution performance. As dissolution rate is generally considered the major limiting step in the oral absorption of poorly soluble drugs, the improved dissolution of RTN supports the potential of βCPCD as a promising carrier to enhance its biological performance.

The release of RTN from the polymeric matrix was evaluated using the dialysis method and the resulting profile is shown in Fig. 3. The rapid diffusion of the free RTN across the membrane and its accumulation in the dialysis medium confirm the suitability of the selected membrane for the test, with nearly 100% of the drug permeating within 7 h. In

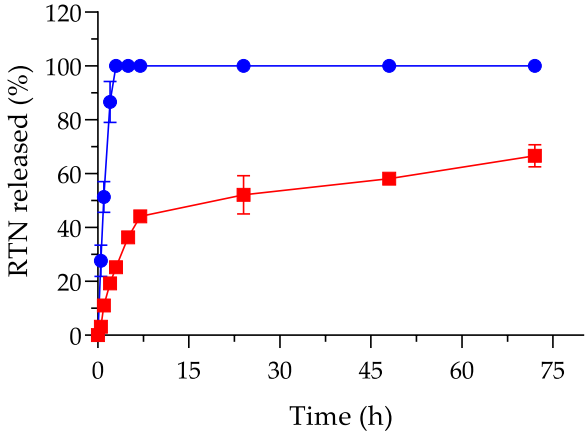


Fig. 3. *In vitro* release profiles of free RTN (circles, blue line) and RTN from the polymeric matrix (squares, red line). Results are expressed as mean values of three different experiments ± SD. The release from the complex was significantly different compared to free RTN, according to one-way ANOVA followed by Bonferroni's post hoc test (***$p < 0.001$).

contrast, the complex exhibited a sustained release profile characterized by two distinct phases. A burst effect occurred within the first 7 h of the beginning of the experiment, with approximately 46% (w/w) of RTN released. This was due to RTN being adsorbed onto the polymer surface or being included within the βCD unit that was exposed at the outer interface. After that, a slower release was observed due to the cross-linked polymer architecture promoting gradual diffusion of the drug through its interstitial space.

The host–guest interaction was investigated through phase solubility studies (Fig. 4). The diagram, obtained by plotting βCPCD concentration (1–10 mg/mL) against the concentration of solubilized RTN, revealed a linear increase in RTN solubility with rising polymer content (A_L-type diagram). This behavior reflects the pronounced solubilizing effect of the polymer, arising from the contribution of multiple concurrent mechanisms (Haimhoffer et al., 2021).

UV–Vis titration studies (Fig. 5) corroborated these findings. Free RTN exhibited characteristic absorption bands at 256 nm ($\pi \rightarrow \pi^*$ transition of the phenyl moiety, A ring) and 352 nm (benzene ring of the pyrocatechol unit, B ring (De Gaetano et al., 2024c), as well as a weak band at ~ 300 nm assigned to the C ring (Zvezdanovic et al., 2012).

Progressive addition of βCPCD caused a hyperchromic shifts in both absorption bands, and a red shift of 2 nm and 4 nm for the first and the second band, respectively. This behavior highlights the interactions between RTN and the polymer, producing changes in the microenvironment of the RTN chromophores. A previous study performed by Calabrò et al. (Calabrò et al., 2005) demonstrated a red shift of RTN bands when they were complexed with monomeric βCD. This was due to displacement of the chromophore from a hydrophilic environment to the hydrophobic βCD cavity, resulting in the formation of hydrophobic and/or van der Waals interactions. However, the same authors observed an opposite influence on the intensity of the bands; that is a hypochromic effect rather than a hyperchromic effect. This different trend suggests additional interactions between RTN and the crosslinked polymeric network, beyond simple host–guest interaction. These interactions are probably hydrogen bonds with PEG linker, which may further contribute to the modification of RTN electronic environment. Together, these interactions explain the strong affinity of βCPCD for RTN and account for the substantial increase in its aqueous solubility observed in phase solubility studies.

The RTN/βCPCD complex was further characterized using ^{1}H NMR spectroscopy (Supplementary Figs. S1 and S2), with a focus on the aromatic protons of RTN as sensitive indicators of changes in the molecular environment upon complex formation. Comparing the spectra of free RTN and the RTN/βCPCD complex (Fig. 6) revealed modest downfield shifts of between 0.06 and 0.15 ppm, for all the aromatic protons of the flavonol core (Table 1). These shifts are consistent with

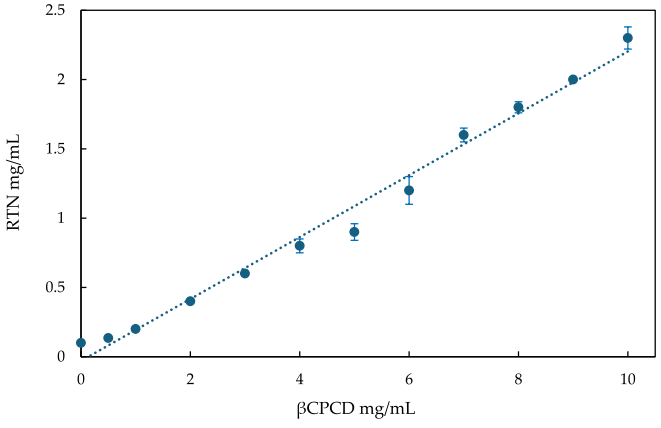


Fig. 4. Phase solubility diagram of RTN with increasing βCPCD concentrations in water at 25.0 ± 0.5 °C. Experiments were performed in triplicate ± SD. Error bars, if not visible, are within the symbols.

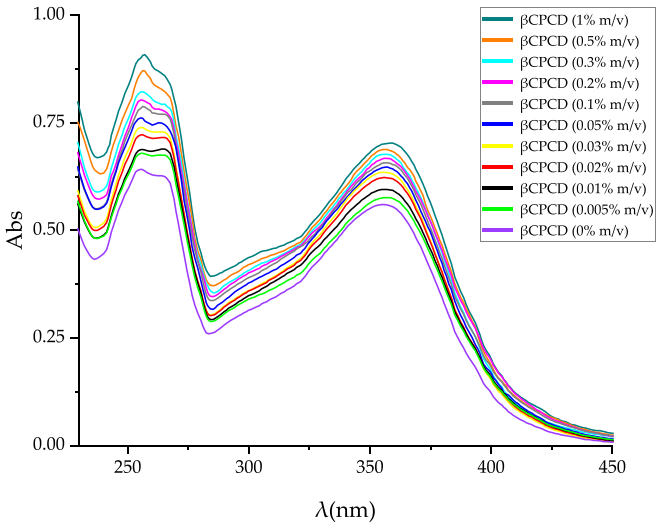


Fig. 5. UV–Vis spectra of free RTN and RTN with increasing βCPCD concentrations in MeOH/water (80:20, v/v) at 25.0 ± 0.5 °C. Experiments were performed in triplicate.

the deshielding effects that arise from changes in the local electronic environment when the molecule interacts with the polymeric matrix.

Small upfield shoulders were detected near the H3, H4, and H5 signals (red line, Fig. 6), suggest that a fraction of RTN molecules is effectively accommodated within βCD cavity, while most remain loosely associated within the three-dimensional network. The absence of additional peaks for H1 and H2 supports their exclusion from the βCD cavity. Overall, the NMR data support a heterogeneous binding situation in which RTN is partially included, which is consistent with the formation of a supramolecular RTN/βCPCD assembly.

Although 2D NOESY/ROESY experiments were performed, no diagnostic intermolecular cross-peaks were identified, presumably because of the heterogeneous and dynamic nature of the polymeric βCPCD system and the partial inclusion of RTN. Within our polymeric βCPCD system, only a small fraction of RTN is likely to be accommodated within the CD cavities; the rest interacts more loosely within the PEG network. Under such heterogeneous and dynamic conditions, the population of clearly included species is insufficient to generate observable NOESY/ROESY cross-peaks, consistent with the absence of diagnostic signals. Such limitations in complex, non-discrete systems have been discussed in the context of cyclodextrin-based supramolecular assemblies and cross-linked cyclodextrin polymers (Conte et al., 2024; Haouas et al., 2023).

3.2. *Aggregation behavior and colloidal properties*

It has been demonstrated that CDs can self-assemble in an aqueous solution to form nanoaggregates (Bleta et al., 2018; Stancanelli et al., 2012) which can permeate biological membranes more effectively than free CDs (Muankaew et al., 2020; Ryzhakov et al., 2016). Therefore, it is important to investigate the ability of βCPCD to form nanoaggregates and to evaluate how the RTN complexation influence this behavior. To this aim, size and zeta potential measurements were carried out on aqueous solutions containing increasing concentrations of free βCPCD or complexed with RTN (Tables 2 and 3).

DLS analysis of free βCPCD (Table 2) revealed a bimodal size distribution showing two distinct populations: i) a small population of species with a diameter of around 15 nm, likely corresponding to unassociated polymer chains; and ii) a large population of supramolecular aggregates with a diameter in the range of 75–114 nm, due to the self-assembling of polymeric chains. This bimodal distribution is characteristic of self-assembling CD polymers and reflects a dynamic

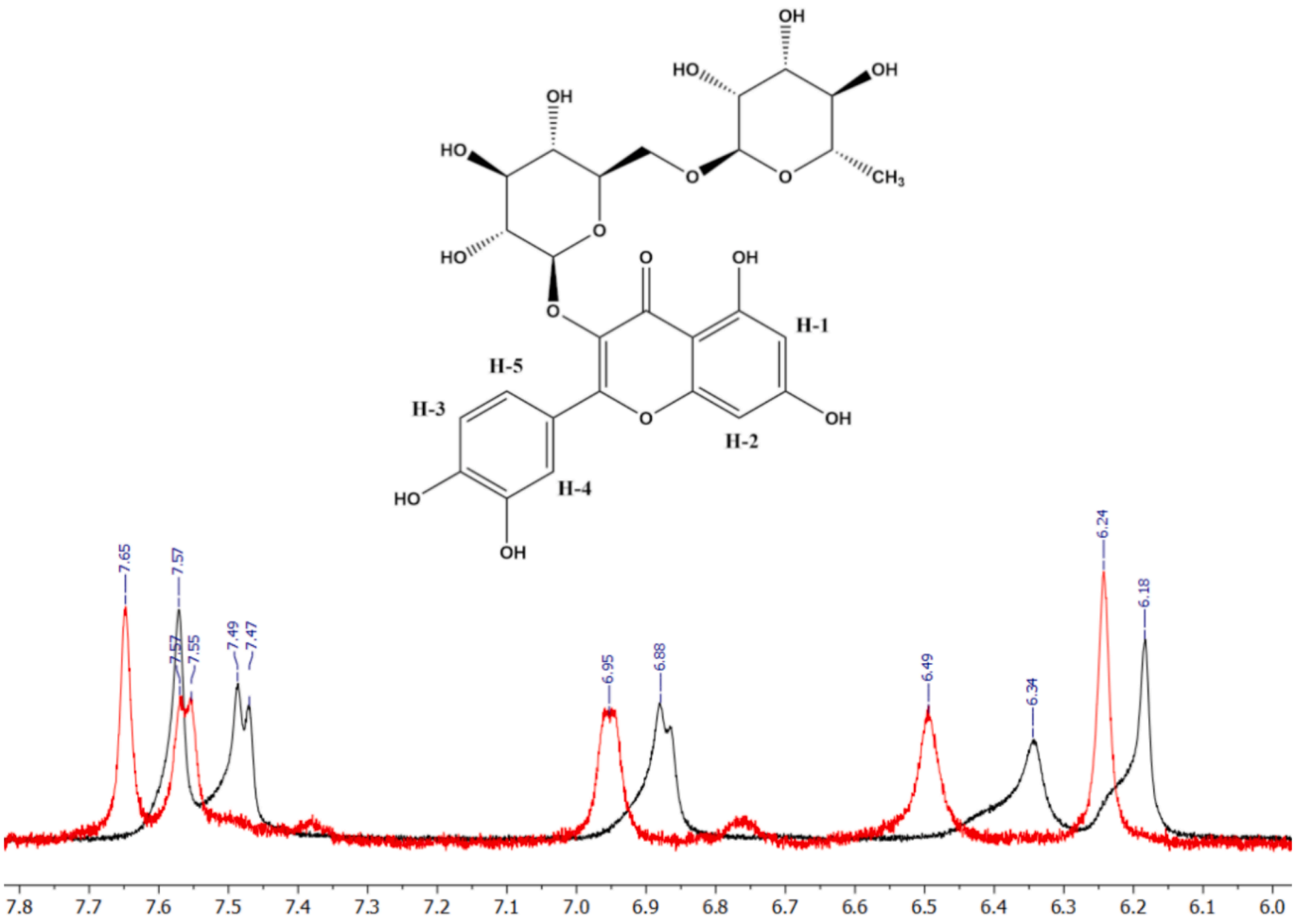


Fig. 6. Comparison of ^{1}H NMR spectra of free RTN (black line) and RTN/βCPCD complex (red line) in D_2O/CD_3OD (80:20, v/v) mixture at 7.8–6.0 ppm.

Table 1
Chemical shifts (*δ*, ppm) of aromatic protons of RTN before and after complexation with βCPCD.

Proton Assignment	Free RTN (*δ*, ppm)	RTN/βCPCD Complex (*δ*, ppm)	Δδ[a] (ppm)
H-1	6.18	6.24	+0.06
H-2	6.34	6.49	+0.15
H-3	6.84	6.95	+0.11
H-4	7.48	7.56	+0.08
H-5	7.57	7.65	+0.08

[a] Dδ = δRTN − δRTN/βCPCD.

equilibrium between the free chains and the corresponding aggregates (Kawano et al., 2015). This type of distribution inherently leads to relatively high PI values, as the mathematical model assumes a unimodal distribution. Thus, the polydispersity index (PI) values obtained for our systems, ranging from 0.29 to 0.47, represent their heterogeneous supramolecular nature.

As βCPCD concentrations increased, aggregates gradually grew in size, passing from approximately 76 nm to 114 nm at the highest polymer concentration. Meanwhile, the sizes of unassociated chains remained relatively unchanged.

This growth of the aggregates was accompanied by a reduction in zeta potential to less negative values, from −12.27 mV at the lowest concentration to −6.87 mV at the highest. Although this decrease resulted in reduced electrostatic repulsion, no visible signs of macroscopic aggregation were observed. Stability studies of the formulations, conducted over a period of 1 month, revealed no significant changes in size or zeta potential, thus confirming the stability of the systems within the studied concentration range.

Table 2
Hydrodynamic diameters (D_H), zeta potential values (ζ) and polidispersity index (PI) of nanoaggregates of free βCPCD.

Concentration (%, m/v)	D_H (nm) ± S.D. Peak 1	D_H (nm) ± S.D. Peak 2	PI (%) ± S.D.	ζ (mV) ± S.D.
0.1	15.72 nm ± 3.50	75.87 nm ± 7.13	0.29 ± 0.09	−12.27 ± 8.26
0.2	15.73 nm ± 2.00	76.42 nm ± 6.85	0.31 ± 0.05	−12.19 ± 9.94
0.3	12.21 nm ± 0.93	81.39 nm ± 9.05	0.33 ± 0.04	−11.72 ± 6.95
0.4	10.78 nm ± 6.15	83.67 nm ± 3.17	0.33 ± 0.04	−11.25 ± 6.62
0.5	11.39 nm ± 0.54	85.17 nm ± 8.78	0.34 ± 0.02	−11.17 ± 4.83
1	11.61 nm ± 0.76	85.71 nm ± 7.03	0.34 ± 0.06	−9.63 ± 4.96
1.5	15.04 nm ± 2.83	87.43 nm ± 2.99	0.44 ± 0.02	−9.56 ± 3.98
2	14.58 nm ± 3.60	94.46 nm ± 5.12	0.46 ± 0.01	−7.05 ± 4.93
2.5	13.80 nm ± 5.23	114.10 nm ± 22.23	0.47 ± 0.10	−6.87 ± 4.89

Complexation with RTN produced larger aggregates than free βCPCD at equivalent concentrations (Table 3), in the range of 0.1–1.5% (m/v). At higher concentrations (2% and 2.5%, m/v) size measurements are

Table 3
Hydrodynamic diameters (D_H), zeta potential values (ζ) and polidispersity index (PI) of nanoaggregates of the RTN/βCPCD inclusion complex. The concentration refers to βCPCD.

Concentration (%, m/v)	D_H (nm) ± S.D. Peak 1	D_H (nm) ± S.D. Peak 2	PI (%) ± S.D.	ζ (mV) ± S.D.
0.1	12.51 nm ± 0.61	81.48 nm ± 4.42	0.31 ± 0.10	−10.56 ± 5.66
0.2	14.46 nm ± 2.71	81.97 nm ± 10.63	0.34 ± 0.05	−10.05 ± 5.52
0.3	14.73 nm ± 3.76	82.51 nm ± 7.45	0.37 ± 0.02	−9.83 ± 6.94
0.4	13.88 nm ± 3.54	82.68 nm ± 3.32	0.37 ± 0.02	−7.13 ± 6.34
0.5	11.35 nm ± 1.94	93.95 nm ± 4.58	0.39 ± 0.03	−5.84 ± 5.58
1	17.54 nm ± 3.79	99.93 nm ± 3.08	0.43 ± 0.04	−5.43 ± 4.66
1.5	18.12 nm ± 4.57	114.41 nm ± 5.81	0.46 ± 0.02	−5.21 ± 3.69
2	N.D.	N.D.	N.D.	N.D.
2.5	N.D.	N.D.	N.D.	N.D.

unreliable. The increase in size compared to the free polymer can be attributed to the altered dynamic self-assembly caused by the interaction of RTN with the polymeric network. It should be noted that βCPCD consist of βCD units interconnected by flexible PEG chains. During self-assembly, βCPCD chains physically interact to delimit an interstitial free volume, the size of which depends on the arrangement of the individual chains in space.

Thus, the presence of RTN within both the βCD cavity and the polymeric network can modify the spatial arrangement of the flexible segments, thereby increasing the free volume in the network and enlarging the aggregates. Furthermore, RTN is partially absorbed onto the aggregate surface and can increase the hydrodynamic radius. Exposed RTN also influences zeta potential values. Its superficial allocation alters the charge distribution on the surface, reducing the values in comparison to the free aggregates.

At polymer concentrations above 1.5% (m/v), RTN appears to induce substantial heterogeneity in the system, thereby preventing size and zeta potential measurements. On the other hand, increasing βCPCD concentration also increases the amount of RTN present in the solution, suggesting a stronger alteration to the polymer's dynamic self-assembly. The physical stability of the samples in the 0.1–1.5% (m/v) range was evaluated over a period of 1 month. No relevant changes in size or zeta potential values were observed.

3.3. At solid-state characterization of the RTN/βCPCD inclusion complex

Thermogravimetric analysis (TGA) was performed to evaluate the solid-state properties and thermal stability of the lyophilized RTN/βCPCD complex in comparison with RTN/βCPCD physical mixture, free RTN and βCPCD polymer alone. The resulting TGA curves, which were recorded in the temperature range of 25–800 °C, are shown in Fig. 7.

Free RTN exhibited a characteristic four-stage degradation profile (da Costa et al., 2002). The initial mass loss of approximately ~ 8% between 30 and 120 °C was attributed to the loss of adsorbed water. The thermal decomposition of the bioflavonoid began at 260 °C, proceeding through two distinct phases to leave a residual mass of around 38%. This behavior is consistent with the known thermal instability of RTN, which undergoes oxidative and structural breakdown at elevated temperatures. The thermal degradation of the free polymer started at 280 °C and proceeded in two stages. The first stage was attributed to soft PEG degradation, while the second stage was attributed to rigid CD units. This process led to a final residue of approximately 6%. Both the RTN/βCPCD complex and the RTN/βCPCD physical mixture displayed an initial weight loss due to water desorption. Notably, the physical

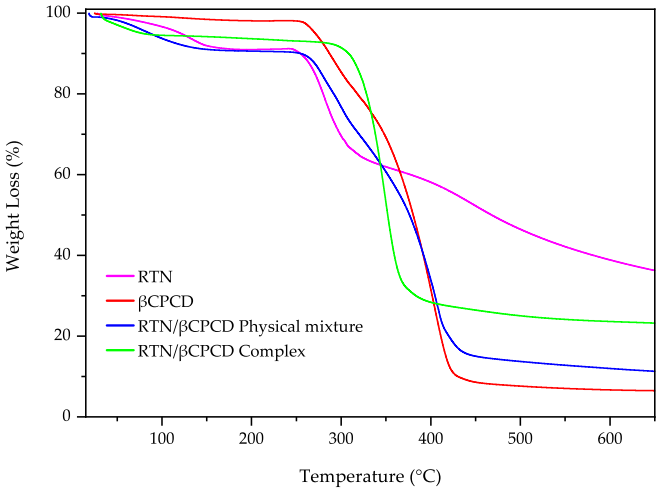


Fig. 7. TGA curves of the RTN/βCPCD complex (green line) compared to free components RTN (purple line) and βCPCD (red line) and their physical mixture (blue line).

mixture exhibited pronounced hygroscopic behavior, with weight loss occurring below 140 °C. In contrast, the complex demonstrated marked improvements in the thermal stability of both RTN (~50 °C) and βCPCD (20 °C), with the onset decomposition shifted to a higher temperature (300 °C), compared to the free polymer and the physical mixture. The mass loss profile also followed a more gradual and linear pattern. This delayed degradation suggests that complexation with βCPCD enhances the RTN's structural resilience by restricting its molecular mobility and shielding it from early thermal breakdown. The stabilization effect is likely due to hydrophobic interactions between the RTN and the internal cavity of the CD, as well as hydrophilic interactions within the polymeric network. These interactions provide a protective microenvironment that reducces the impact of external thermal stress. These findings highlight the potential of βCPCD as a stabilizing carrier for RTN, supporting its use in formulations requiring enhanced thermal resistance.

3.4. Morphological examination

Fig. 8 shows SEM micrographs of the βCPCD polymer and its RTN complex. We observed a predominantly spherical morphology, with particle sizes ranging from a few hundred nanometers to 1–2 μm. However, Dynamic Light Scattering (DLS) analyses indicate a primary hydrodynamic population of approximately 100 nm (see Tables 2 and 3). The predominant particle population lies within the 50–100 nm range, although particles with bigger sizes up to 10 μm are also present. The presence of larger structures may be attributed to aggregation phenomena occurring during sample preparation, such as drying or freeze-drying on a silicon support. Solvent removal generates surface tension forces that favor the coalescence of nanoaggregates into larger clusters. This behavior was documented in both iCD-based systems (Swaminathan et al., 2016; Tejashri et al., 2013) and in generic polymeric nanoparticles subjected to drying or freeze-drying processes (Garms et al., 2021; Picco et al., 2021).

A further important aspect concerns the resilience of the samples under the electron beam. While the polymer "blank" shows signs of early degradation or image instability at high magnifications, the RTN/βCPCD complex exhibits increased structural stability. This suggests that the inclusion of the host molecule within the CD cavities and in the interstices of the polymer network may contribute to mechanical and thermal reinforcement, reducing the free volume of the matrix and improving the locally induced energy dissipation of the electron beam. These effects are consistent with previous studies on the physical-chemical stability of polymer–drug complexes (Trotta et al., 2012a;

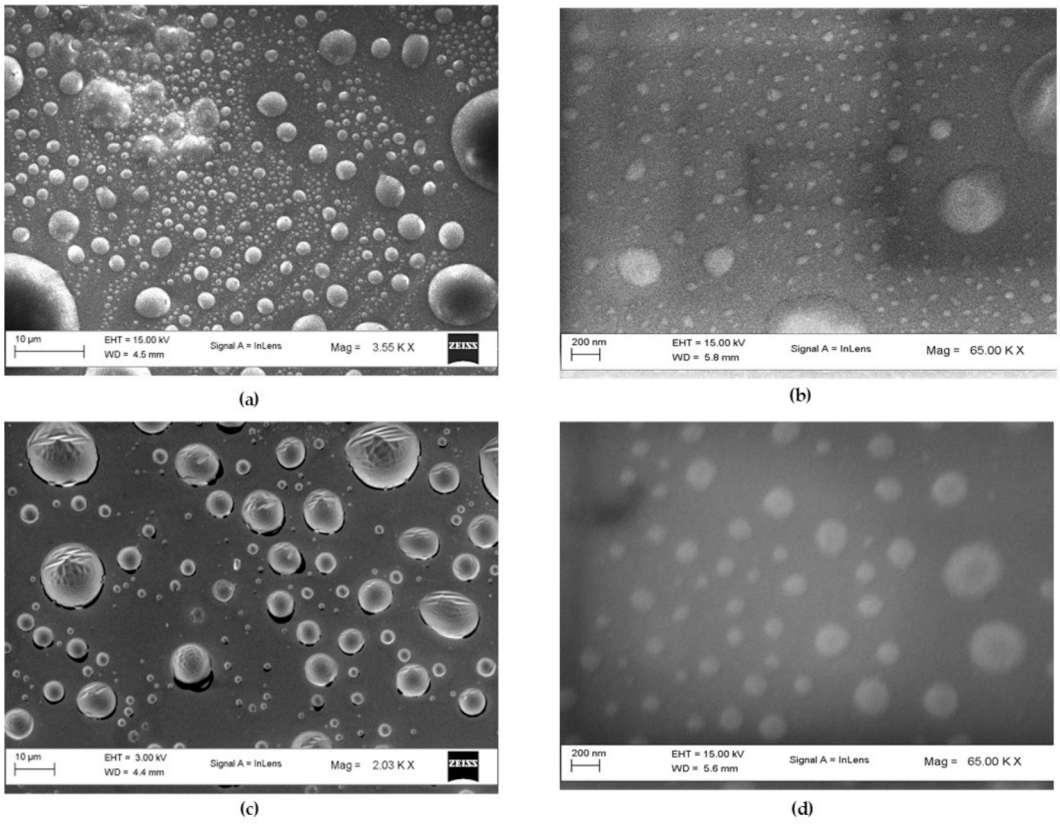


Fig. 8. SEM images of RTN/βCPCD complex (a,b) and βCPCD alone (c,d) at different magnification.

van de Manakker et al., 2009).

3.5. Molecular characterization and modeling

A μ-Raman analysis was carried out to assess the capability of βCPCD to interact with RTN based on the characterization of the intermolecular interactions involved in the complexation pathway. The adopted approach, proven effective in prior studies of similar systems (Cannavà et al., 2016; Sajeesh and Sharma, 2006; Venuti et al., 2019, 2017; Zhao et al., 2020), consisted in monitoring significant spectral changes of characteristic vibrational bands of free RTN when embedded within the βCPCD structure, starting from the comparison of the vibrational features exhibited by the RTN/βCPCD complex with respect to those of the physical mixture (a simple blending of RTN and βCPCD without any complexation) and single components.

Fig. 9a shows the comparison of the μ-Raman spectra collected for RTN, βCPCD, RTN/βCPCD physical mixture and RTN/βCPCD inclusion complex, in the 650—1800 cm^{-1} wavenumber range, at T = 300 K.

As far as RTN and βCPCD are concerned, a detailed spectral assignment is given in the supplementary materials (see Table S1 and S2, respectively). Concerning the μ-Raman spectrum of the physical mixture (green line in Fig. 9a), it exhibits vibrational bands corresponding to

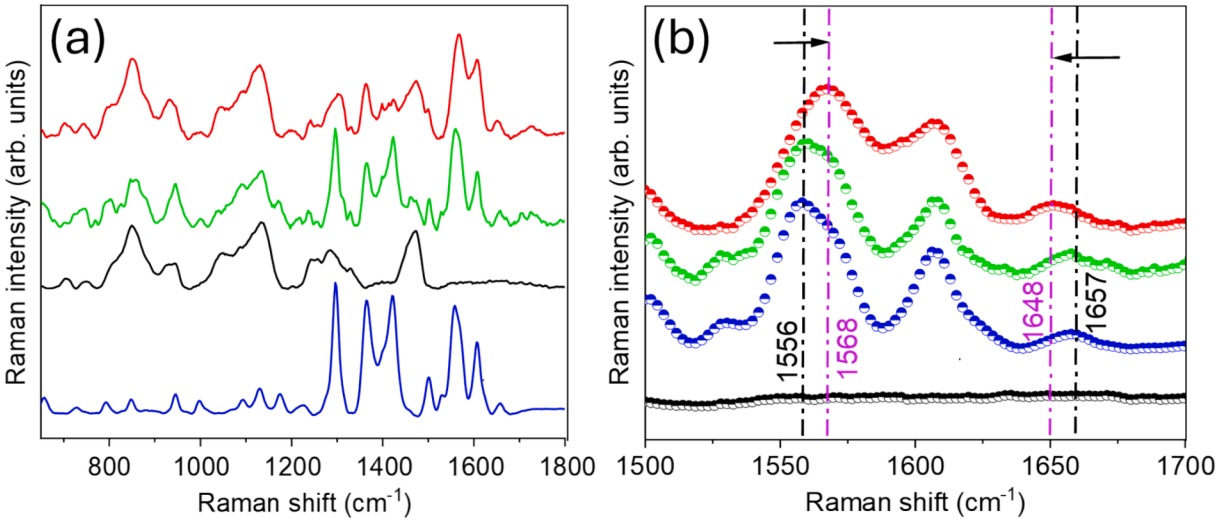


Fig. 9. (**a**) μ-Raman spectra, in the 650—1800 cm^{-1} range, of RTN (blue line), βCPCD (black line), RTN/βCPCD physical mixture (green line) and RTN/βCPCD inclusion complex (red line), at T = 300 K. (**b**) Comparison, in the 1500 – 1700 cm^{-1} range, of the obtained μ-Raman profiles.

each individual component, with no significant band broadening or frequency shifts, indicating the absence of specific intermolecular interactions between components, as expected. Conversely, the μ-Raman spectrum of the RTN/βCPCD complex (red line in Fig. 9a) showed significant spectral changes when RTN is included in the host βCPCD matrix. In particular, the attention was paid on spectral modifications occurring in the region extending between 1500 and 1700 cm^{-1} that, being devoid of vibrational contributions from βCPCD alone, can be directly inferred to the inclusion process of the drug within the βCPCD site. From detailed analysis of such frequency region (Fig. 9b), a blue-shift of the characteristic C=C stretching mode of benzene and dihydroxyphenyl rings of RTN, with respect to the free drug, can be clearly observed. In particular, the centre-frequency of the corresponding band moves, going from the spectrum of the physical mixture to that of the inclusion complex, from ~ 1556 cm^{-1} up to ~ 1568 cm^{-1}, providing an experimental evidence of the establishment of drug-βCPCD intermolecular interactions involving the participation of the benzene and/or dihydroxyphenyl ring in the complexation pathway.

In addition, the analysis of the 1500–1700 cm^{-1} range also evidenced a red-shift of the contribution centred at ~ 1657 cm^{-1}, related to the carbonyl stretching mode of the heterocyclic ring of RTN. As well known, the C=O stretching vibration is highly sensitive to variations in the electrostatic environment and to conjugation effects experienced by the carbonyl group (Venuti et al., 2017). In our case, the observed red-shift reasonably implies the establishment of new intermolecular hydrogen bonds, involving either oxygen atoms of carbonyl groups at C6 position or nearby oxygen-containing moieties, both yielding to a redistribution of the electron density of the flavonoid backbone, which favors the stabilization of the complex.

To highlight further significant spectral marker of the RTN/βCPCD complex formation, FTIR-ATR measurements were carried out. Similarly to the μ-Raman approach, the analysis consisted in monitoring spectral modifications experienced by some characteristic absorption bands of the free drug upon the activation of intermolecular interactions driving the RTN complexation within the βCPCD environment.

Fig. 10a reports the FTIR-ATR spectra of RTN, βCPCD, RTN/βCPCD physical mixture and RTN/βCPCD complex, acquired at room temperature, in the 750 – 4000 cm^{-1} wavenumber range.

A complete spectral assignment of the FTIR-ATR bands related to RTN and βCPCD is reported in the Supplementary Materials (Table S3 and Table S4, respectively). Interestingly, the FTIR-ATR spectrum of the RTN/βCPCD complex (red line in Fig. 10a) exhibited subtle yet clearly detectable spectral variations with respect to both the physical mixture (green line in Fig. 10a) and individual components (blue and black lines in Fig. 10a, respectively). These are particularly evident in the 1500—1600 cm^{-1} spectral region which, being devoid of vibrational contributions originating from the βCPCD alone, constitutes an excellent candidate to highlight modifications as a consequence of complexation. Fig. 10b displays the comparison of the measured FTIR-ATR spectra for all the investigated samples in the 1400—1700 cm^{-1} wavenumber range, at T = 300 K. From an inspection of the Figure, vibrational contributions centered falling at ~ 1505 cm^{-1} and ~ 1600 cm^{-1}, assigned to C=C stretching modes of the benzene ring and to C=C stretching vibrations involving the benzene, heterocyclic and dihydroxyphenyl rings of RTN, respectively (see Table S3 in the Supplementary Materials), still detectable in the spectrum of the physical mixture, experience a complete suppression in the FTIR-ATR spectrum of the RTN/βCPCD complex. These findings point out an active participation of the aromatic rings of RTN in the host–guest complexation route, through the establishment of non-covalent intermolecular interactions involving the benzene and dihydroxyphenyl moieties of the flavonoid, thereby corroborating — in agreement with the μ-Raman analysis — the successful encapsulation of RTN within the βCPCD polymeric matrix.

Molecular docking simulations were carried out to investigate the encapsulation geometry and provide additional insights into the host–guest interactions driving the inclusion mechanism. The results of the extra precision (XP) flexible docking method provided 5 different docking poses, each characterized by a docking score ranging from − 2.87 kcal/mol (low-scoring docking XP pose) to − 3.66 kcal/mol (top-scoring docking XP pose). Fig. 11 shows the most favourable geometry for the RTN/βCPCDm structure, identified as the generated top-scoring XP pose.

RTN was found to partially penetrate the βCD cavity, with only a portion of the molecule, primarily the hydroxyphenyl ring of the

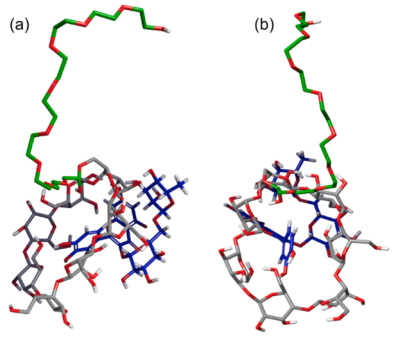


Fig. 11. (a) frontal and (b) side-view of the RTN/βCPCDm docked structure. The blue molecule denotes RTN, the grey one denotes the βCD, while the green one identifies the PEG chain.

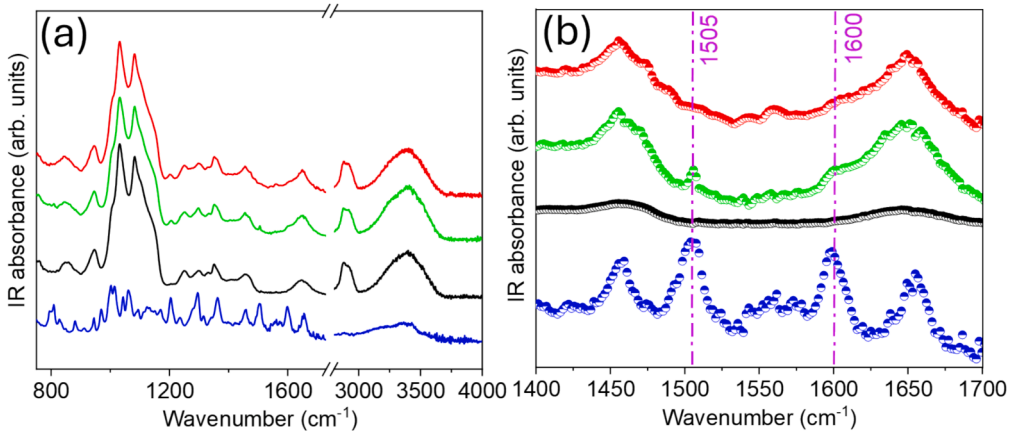


Fig. 10. (**a**) FTIR-ATR spectra, in the 750 – 4000 cm^{-1} wavenumber range of RTN (blue line), βCPCD (black line), RTN/βCPCD physical mixture (green line) and RTN/βCPCD complex (red line), at T = 300 K. (**b**) Comparison, in the 1400—1700 cm^{-1} range, of the collected profiles.

quercetin moiety, accommodated within the hydrophobic core of βCD, as expected due to the large, low-flexible branched structure of RTN. The sugar moiety, highly hydrophilic, extends outside the cavity, thus remaining exposed to the solvent molecules (De Gaetano et al., 2024c) and the rest of the 3D polymeric structure. The PEG chain, oriented away from the cavity, remains flexible to avoid steric hindrance at the entry point.

The stability of the RTN/βCPCDm docked structure turns out to be dependent by several factors including intermolecular hydrogen bonds, hydrophobic forces and electrostatic effects. In particular, the hydrogen atom (H73) of the hydroxyphenyl ring of RTN establishes a strong H-bridge with the βCD oxygen (O30) of the nearest glucopyranose unit (Fig. 12a), characterized by a length of 2.070 Å and a bond angle of 135.030°. At the same time, 4 additional RTN-βCD hydrogen bonds, respectively involving the O (O11) atom of the heterocyclic ring and three hydroxyl group hydrogens of the sugar moiety, *i.e.* the mannopyranosyl and glucopyranosyl rings, provide a "chelating" effect which reinforces the RTN/βCPCD binding in solid state (Fig. 12b).

It is worth noting that the predicted establishment of an H-bridge between the heterocyclic ring of RTN and the macrocycle can be considered as responsible of a redistribution of the electron density surrounding the corresponding moiety, thus corroborating the observed frequency-shift of the C=O stretching mode by μ-Raman spectroscopy as well as the suppression of the C=C stretching mode of the heterocyclic observed FTIR-ATR.

The MM-GBSA method described in section 2.11 was applied to calculate the free energy of binding (ΔG Bind) and the MM-GBSA scores of the docked RTN/βCPCD structure. The results are reported in Table 4.

From MM-GBSA results, of the docked RTN/βCPCD structure shows a favourable free binding energy ΔG Bind of − 30.719 kcal/mol, testifying a strong and thermodynamically stable structure. The RTN/βCPCD host − guest interactions, from a local point of view, are predominantly driven by van der Waals (−15.773 kcal/mol) and lipophilic (−10.301 kcal/mol) forces, which are consistent with the non-covalent encapsulation mechanism characteristic of βCD-based inclusion complexes (Geue et al., 2023; Mahalapbutr et al., 2019; Venuti et al., 2017; Zhang et al., 2012). The hydrogen bonding component of − 3.013 kcal/mol suggests the possible involvement of highly directional interactions between the hydroxyl groups of RTN and the polar moieties located at the CD cavity rim. Interestingly, the free energy of binding deriving from covalent interactions (ΔG Coval) and polar solvation (ΔG Solv) partially counteract the stabilizing factors which foster the RTN/βCPCD formation. In particular, the obtained positive value of the covalent energy contribution (+ 4.417 kcal/mol) is indicative of internal energetic penalties arising from torsional strain within the RTN backbone and local conformational adjustments of the CD scaffold induced by the docked configuration.

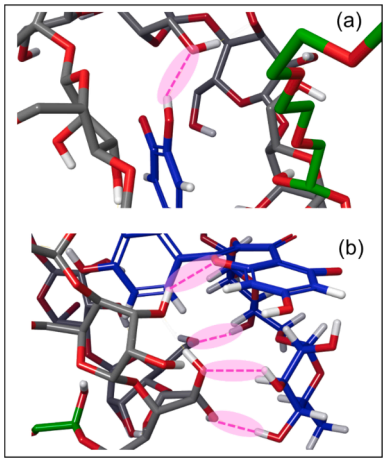


Fig. 12. Detail of the hydrogen bond scheme (purple dashed line) developed in the RTN/βCPCD structure. **(a)**: H-bridge between H73 atom of RTN and O30 atom of βCD; **(b)** H-bonds between O11 atom and three H-atoms of hydroxyl group of the sugar moiety of RTN with βCD.

As reported in literature (Hou et al., 2011), the MM-GBSA values can be used to assess the enthalpy (ΔH Bind) and entropy (ΔS Bind) variation associated to the host–guest" binding, based on the assumption that our simulations involved a single molecular dynamic path. Accordingly, a value of $\Delta H = -21.819$ kcal/mol and of $\Delta S = +0.029$ kcal/mol were obtained, indicating that the formation of the RTN/βCPCD complex is an exothermic, enthalpy-driven, process.

It is worth of note that recent studies on similar CD–polymer architectures used for the delivery of flavonoids demonstrated that docking-derived binding modes and interaction patterns strongly affect the encapsulation stability and downstream pharmacological performances (Malekpour et al., 2025), highlighting the ability of docking metrics to anticipate biological efficacy in complex structures (Emmanuel et al., 2025; Naveed et al., 2026). In our case, the partial encapsulation of the hydroxyphenyl ring of the quercetin moiety of RTN within the βCD cavity was found to be in line with what has been reported in (Almeleebia et al., 2024; Chang et al., 2023; Liu et al., 2022; Mourad et al., 2024; Naeem et al., 2023), which revealed a not complete incorporation of the flavonoid due to its large size. In addition, the dominance of van der Waals and hydrophobic interactions are consistent with literature emphasizing non-covalent host–guest forces as driving factors in CD flavonoid complexes (Fenyvesi et al., 2025). Furthermore, the encapsulation of RTN through the hydroxyphenyl ring was found to be a typical complexation pathway in flavonoid-based CD delivery platforms, despite the steric effect of the two closely arranged sugar groups (Liu et al., 2012; Matteini et al., 2010; Nguyen et al., 2013).

To assess the stability of the RTN/βCPCDm local environment, MD simulations were conducted in an aqueous medium over 40 ns trajectories. Representative MD snapshots captured at specific time intervals (0 ns, 20 ns and 40 ns) are depicted in Fig. 13(a−c).

As observed in Fig. 13(a-c), RTN remains partially accommodated within the βCD cavity of the βCPCDm through the hydroxyphenyl ring of the quercetin moiety over the entire simulation time (40 ns), as predicted by docking simulations. No dissociation events or significant translational displacement of the guest molecule were observed, indicating the formation of a stable complex with no spontaneous separation (Alvira, 2019; Kicuntod et al., 2018; Kou et al., 2024; Minea et al., 2016). For the first 20 ns, minor conformational changes in the βCD toroid can be inferred to local rearrangements of the glucopyranose units upon ligand accommodation, which tend to stabilize till the end of the simulation. Interestingly, over the same time period (first 20 ns), a progressive approaching of the PEG chain toward the βCD cavity, initially pointing outward from the cavity pocket (see Fig. 13a), can be observed, suggesting a cooperative adjustment of the cyclodextrin–polymer architecture rather than an isolated fluctuation. Such process contributes to the overall stabilization of the complex through transient non-covalent interactions and steric confinement effects at the cavity rim (Jitapunkul et al., 2021; Liu et al., 2013; Poonphatanapricha et al., 2021).

The stability of the modeled RTN/βCPCDm complex was further investigated through the root mean square deviation (RMSD) and the radius of gyration (Rg) plots calculated over the entire simulation time, as reported in Fig. 13d and e. As far as the RMSD is concerned, in the case of RTN (blue line in Fig. 13d), a stable dynamical behavior can be deduced by a mean RMSD value of 2.78 ± 0.19 Å, with a temporary dip down to 0.78 ± 0.19 Å (between 21 ns and 23 ns), due to the exploring of energetically-favored transient re-orientations inside the binding site, followed by a stable plateau for $t > 23$ ns, supporting the durability of the RTN/βCPCDm docked arrangement (Naveed et al., 2025; Sadia et al., 2024; Suleman et al., 2024, 2024). Concerning the βCPCDm, the RMSD plot (red line in Fig. 13d) shows significant fluctuations in the first 21 ns of the simulation run, due to the large structural motions

Table 4
MM-GBSA scores (kcal/mol) of the docked RTN/βCPCD docked inclusion complex*.

	ΔG Bind	ΔG Coul	ΔG Coval	ΔG H-Bond	ΔG Hphob	ΔG Solv	ΔG VdW
RTN/βCPCD complex	**−30.719**	−9.111	+ 4.417	−3.013	−10.303	+ 3.024	−15.773

* ΔG Bind: free energy of binding; ΔG Coul: free energy of binding from electrostatic interactions; ΔG Coval: free energy of binding from covalent interactions; ΔG H-Bond: free energy of binding from hydrogen bonding; ΔG Hphob: free energy of hydrophobic interactions; ΔG Solv: free energy of binding from polar solvation; ΔG VdW: free energy of binding from van der Waals interactions.

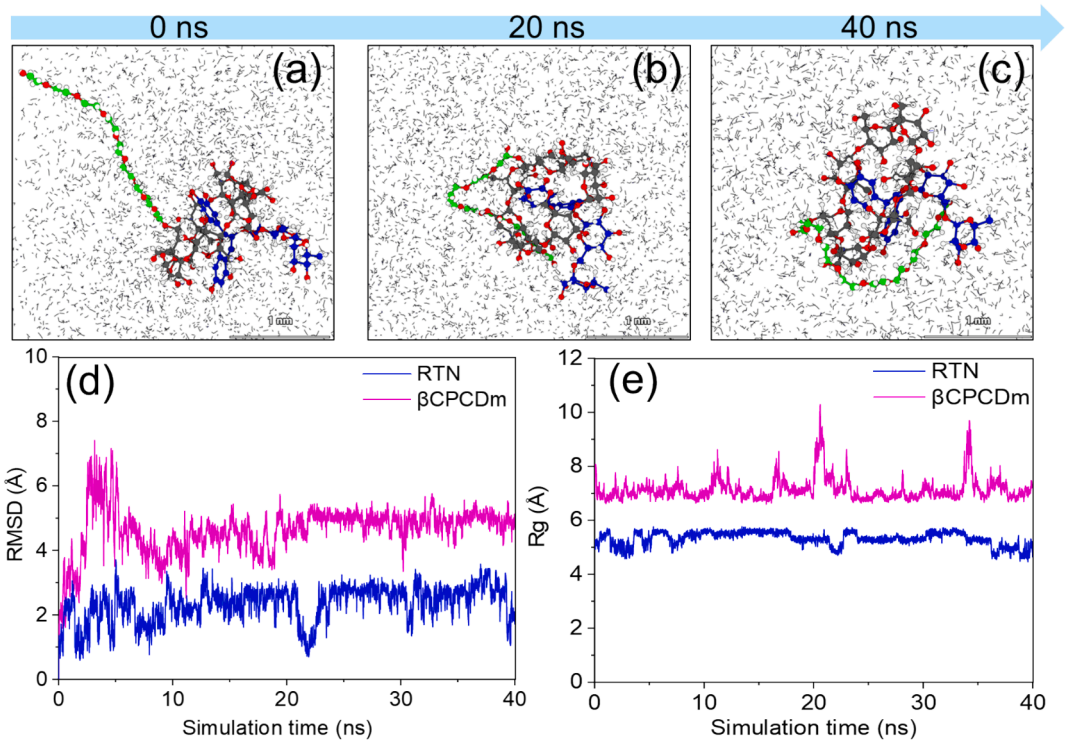


Fig. 13. Representative snapshots depicting the dynamic behavior of RTN (blue molecule) within the cavity of the βCD (grey molecule) of the βCPCDm unit, as predicted by molecular dynamics simulations at, respectively, (**a**) 0, (**b**) 20 and (**c**) 40 ns. For clarity, the PEG chain is highlighted in green for visual representation. (**d**) RMSD and (**e**) radius of gyration (Rg) of RTN and βCPCDm as a function of the simulation time.

related to the high-flexible PEG chain (mostly transient stretching). However, as also revealed by the snapshot analysis, for $t > 22$ ns, a constant trend of the RMSD (mean value of 4.93 ± 0.26 Å) testifies the stabilization of the receptor due to the wrapping of the PEG chain around the CD.

Finally, the Rg trend of both RTN and βCPCDm (Fig. 13e) of the modelled inclusion complex, calculated over the 40 ns-run, further confirms that the inclusion complex holds its integrity and packed architecture, with an Rg mean value of 5.27 Å and 7 Å, respectively (Hassan et al., 2024; Naveed et al., 2025). Slight fluctuations in βCPCDm can be justified considering the flexibility of the βCD rings, which undergo small twisting or puckering motions, as well as in terms the transient contacts, especially for t > 22 ns, between the PEG chain and the macrocycle – which yield to slight expansion/compression the βCD cavity. Interestingly, the remarkable system dynamics favored by the PEG chain aligns with recent results reported in literature for similar systems (Chadha et al., 2011; Fenyvesi et al., 2025) supporting the conclusion that the PEG moiety in the βCPCDm unit not only reduces steric hindrance but also participates in the stabilization of the resulting system.

3.6. Evaluation of tolerability in zebrafish embryos

Given the novelty of the polymer used in this study, a preliminary assessment of its *in vivo* safety profile was essential. With this aim, we evaluated the βCPCD tolerability in zebrafish embryos exposed at polymer concentrations ranging from 0.05-50 mg/mL. In this contest, tolerability was defined as the absence of mortality or abnormality development throughout the exposure period. The concentration range was selected based on studies present in literature which investigated the tolerability of native βCD and PEG in zebrafish embryos. Specifically, Weiss-Errico et al. (2017) (Weiss-Errico et al., 2017) reported that native βCD was well tolerated at concentrations up to 0.164% (m/v), whereas PEG was tolerated at concentrations exceeding 2.5% (m/v) (Maes et al., 2012). The concentrations tested in our study largely encompass the reference values for both compounds, providing a robust preliminary evaluation of βCPCD safety.

Table 5
Mortality rate of zebrafish embryos submitted to different treatments at 72 hpf. The number of embryos for each group is expressed as a percentage of the total embryos (n = 20).

Sample	Concentration (mg/mL)	Mortality (%)
Ctrl	–	0
RTN	0.01–0.1	0
	0.5	50
	1.0	90
RTN/βCPCD *	0.01–1	0
βCPCD	0.05–50	0

* Concentration refers to the amount of RTN within the complex.

In Table 5 we report the results obtained. No mortality of zebrafish embryos was observed up to the highest assayed dose (50 mg/mL), nor did they display developmental abnormalities under stereomicroscopic examination when compared to the control group. Even if additional studies are needed to evaluate the toxicological profile of the polymer, these findings provide clear evidence of the key role exerted by the PEG chains in enhancing *in vivo* tolerability of βCD-based materials, supporting the suitability of the cross-linked βCPCD polymer as a promising platform for drug-delivery applications.

Tolerability of free and complexed RTN was also evaluated (Table 5). Free RTN showed no mortality or abnormality at a concentration up to 0.1 mg/mL. Higher concentrations demonstrated a dose-dependent toxic effect, with embryo mortality reaching approximately 90% at 1 mg/mL dose. Conversely, treatment of embryos with complexed RTN did not induce embryo mortality across a considerably broader concentration range (0.01–1.0 mg/mL), than free RTN, showing its high tolerability in the range of tested concentrations.

The toxicity of free RTN can be related to its very low water solubility. Although RTN was initially dissolved in 0.2% DMSO, upon dilution into aqueous media precipitation or formation of colloidal aggregates occurs (Gillespie et al., 2013; Popa-Burke and Russell, 2014; Waybright et al., 2009), as evidenced by the formation of a visible opalescence in the fresh prepared samples of RTN, specially at the high concentrations. These solid particles can induce mechanical stress to embryos or impair oxygen exchange, producing embryotoxicity. In contrast, RTN/βCPCD complex remains fully water-soluble and stable in embryo medium, preventing precipitation and ensuring that a significant higher amount of RTN remains in solution in the microenvironment of zebrafish embryos. This is an important result because it demonstrates that βCPCD not only improves water solubility of RTN but also mitigates nonspecific, formulation-related toxicity, expanding its applicability *in vivo* models.

3.7. Antiangiogenic activity in zebrafish embryos

In recent years, zebrafish embryos have gained significant attention as an *in vivo* model for predicting not only the toxic effects of bioactive compounds, but their antioxidant, or antiangiogenic activity also. Their optical transparency allows for direct observation of vascular network development, providing a valuable tool for studying angiogenesis. Quantitatively, this process can be monitored by measuring the activity of EAP, an enzyme released by endothelial cells during vessel growth. Due to its direct correlation with vascular formation, alkaline phosphatase activity is widely recognized as a biomarker of angiogenesis (Hu et al., 2023; Huang et al., 2016; Jiang et al., 2023; Liang et al., 2017).

The effect exerted on EAP activity by the different samples was assessed at the safe concentrations range, as determined by the previous tolerability evaluation. Specifically, 0.01–0.1 mg/mL for free RTN, 0.01–1 mg/mL for complexed RTN and 0.05–50 mg/mL for free βCPCD). The results were compared to the inhibitory effect exerted by 2-methoxyestradiol, an endogenous 17β-estradiol metabolite with well-documented antiangiogenic and antitumor properties, known to inhibit enzyme activity by approximately 50% (Mooberry, 2003).

As expected, the inhibitory effect of βCPCD on vascular growth was negligible at all assayed concentrations, showing a maximum inhibition of 0.98% at the highest concentration tested (50 mg/mL). This result was consistent with its intrinsic biocompatibility and demonstrated the absence of direct effects on vascular development within the assayed concentration range.

The percentage inhibition of EAP activity induced by free and complexed RTN is shown in Fig. 14. Both free RTN and RTN/βCPCD exhibited dose-dependent antiangiogenic effects. However, due to the limited solubility, RTN can be tested in a narrow range of concentration, showing a mild inhibition, that reached about 13% at the highest concentration (0.1 mg/mL). Complexation of RTN with βCPCD permitted to assay a very broader concentration range (0.01–1. mg/mL), obtaining at the highest dose an inhibition level of 42.14%, mostly comparable to 2-methoxyestradiol (50%). Complexation enables the solubilization of a higher amount of RTN, which remains fully water-soluble and stable in the microenvironment of zebrafish embryos. This allows treatment at higher effective doses than would be possible with free RTN, ultimately enhancing its biological efficacy.

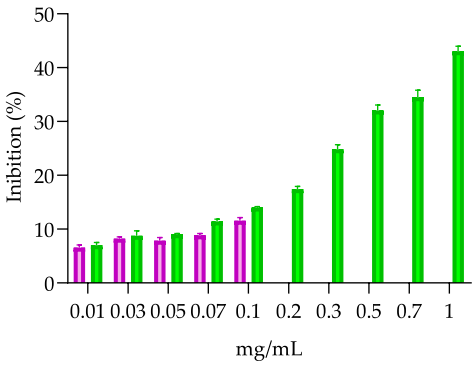


Fig. 14. Dose–dependent inhibition of antiangiogenic activity exhibited by RTN (pink) and RTN/βCPCD complex (green) within the concentration range of 0.01–1 mg/mL.

The antiangiogenic activity of RTN/βCPCD complex was further confirmed through the alkaline phosphatase (ALP) staining assay, in comparison with free RTN. The effects exerted by different samples on intersegmental vessel (ISV) growth are shown in Figs. 15 and 16 in comparison with the positive control. A clear dose-dependent effect was observed in Fig. 15 D-F for RTN/βCPCD complex, which produced, at the highest concentration tested (1 mg/mL), a significant reduction in the total length, number and area of the ISV (28.5%, 31% and 45.75%, respectively) as compared to negative control (Fig. 15A). This inhibitory effect was almost comparable to that exerted by the positive control (2-methoxyestradiol) (Fig. 15B), which reduced the total length, number and area of ISV of 35.9%, 40.5% and 55.3%, respectively) (Fig. 16). Notably, free RTN produced only a minimal inhibitory effect on IVS growth (Fig. 15C and Fig. 16), confirming its limited antiangiogenic effects in the absence of an efficient delivery system.

4. Conclusions

This study developed a supramolecular delivery system based on βCPCD (a highly hydrophilic, crosslinked βCD-PEG polymer) to complex RTN, aiming to improve its solubility and antiangiogenic activity. Complexation with βCPCD markedly improved the biomolecule's water solubility (by about 50-fold) and dissolution rate (50% within 5 min, with total dissolution within 60 min). These findings are due to the polymer's architecture, which allows the RTN moiety to be included in the βCD cavity and accommodated in the interspatial pores of the cross-linked network, as supported by UV–Vis and NMR spectroscopy. Due to this specific accommodation, the polymer produced a sustained release of RTN. Morphological examination confirmed the polymer's porous structure, and thermogravimetric analysis revealed the RTN complex's enhanced thermal stability.

μ-Raman and FTIR-ATR spectra revealed distinct shifts and/or suppressions in characteristic vibrational bands of RTN upon complexation, confirming molecular interactions with βCPCD. Additionally, preliminary molecular docking approaches assessed the optimal inclusion complex geometry for a local scenario involving a single RTN and βCD-PEG unit within the simulation environment. The structural stability of this scenario was then evaluated via molecular dynamics (MD) simulations. More complex and highly demanding simulations will be implemented in a future dedicated work to incorporate the entire polymeric architecture of the host. This will allow for the evaluation of the long-range cooperative effects and conformational flexibility under

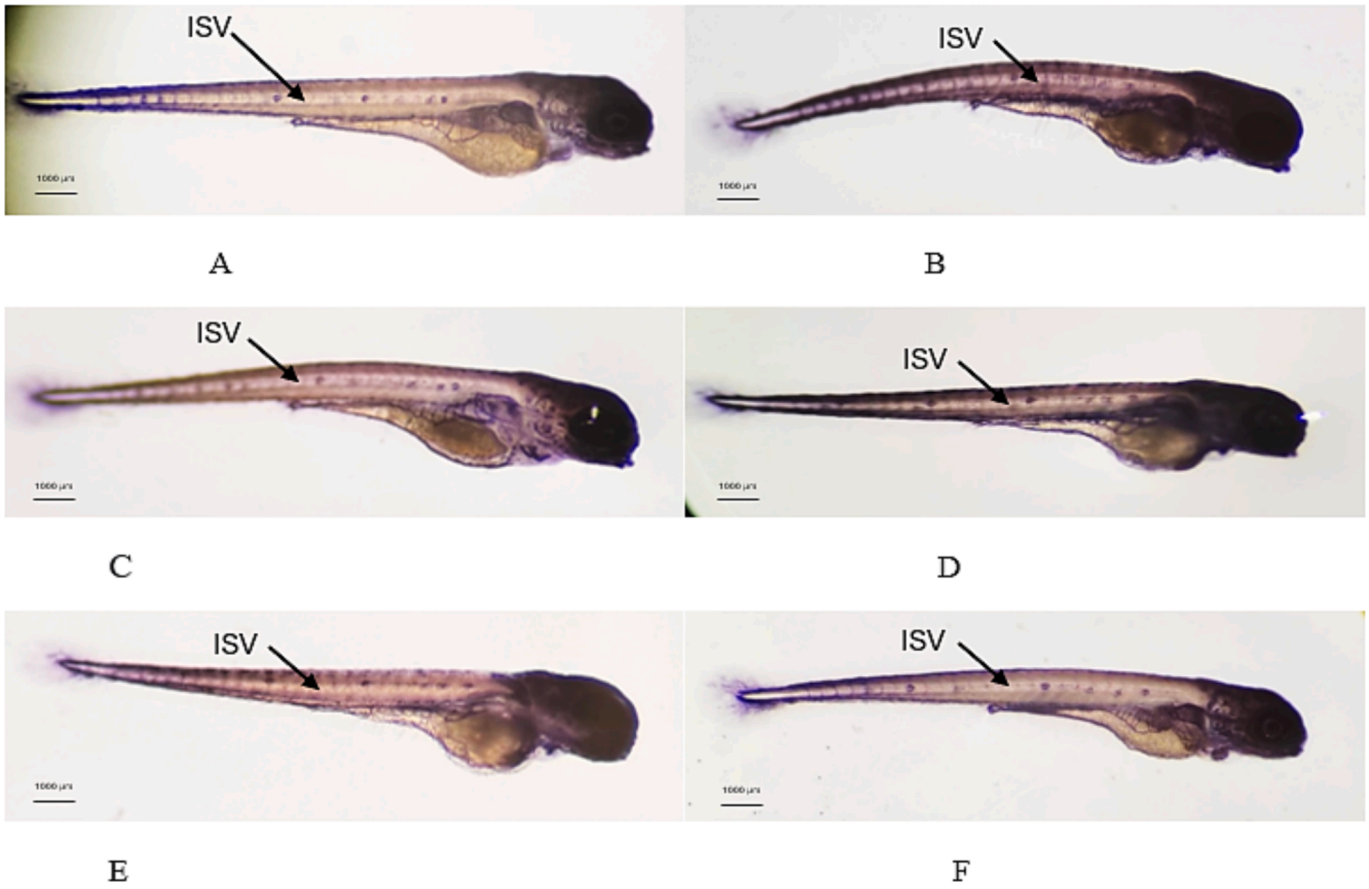


Fig. 15. *In vivo* angiogenesis in the zebrafish embryos: lateral view of alkaline phosphatase-stained embryos at 72 hpf. A = control; B = 2- Methoxyestradiol (0.006 mg/mL); C = RTN (0.1 mg/mL); D = RTN/βCPCD (0.1 mg/mL); E = RTN/βCPCD (0.5 mg/mL); F = RTN/βCPCD (1 mg/mL). Images were captured with a stereomicroscope (SMZ-171 Series, Motic) equipped with a digital camera (Moticam® 5 plus). ISV = intersegmental vessel. Scale bar: 1000 μm.

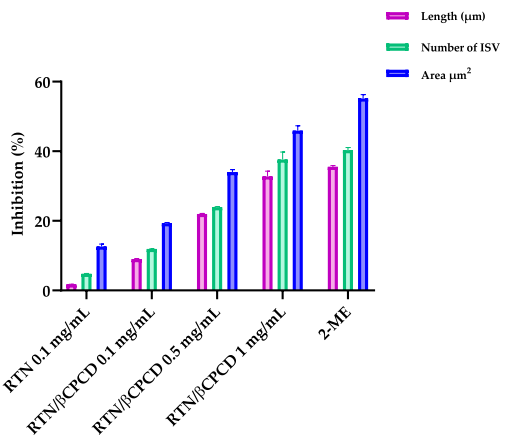


Fig. 16. Quantitative results of treatment with free RTN, RTN/βCPCD complex and 2- methoxyestradiol (2-ME) on intersegmental vessel (ISV) growth in alkaline phosphatase (ALP) stained zebrafish embryos at 72 hpf. The total intersegmental vessel (ISV) length and area, ISV number were measured using Motic Images Plus 3.1 software. Results were expressed as percentage of inhibition (%) of the treated groups compared to negative control group (100% of activity). Data represents the mean ± SD; $n = 3$ independent replicates with 5 embryos in each replicate. According to oneway ANOVA followed by Dunnett's post hoc test, all RTN/βCPCD formulations exhibited extremely significant differences compared with free RTN (****$p < 0.0001$).

conditions that more closely resemble the real RTN/βCPCD environment.

In zebrafish (*Danio rerio*) embryos, βCPCD showed excellent biocompatibility, without mortality or abnormalities up to 50 mg/mL dose. Complexation of RTN with the polymer mitigates its nonspecific, formulation-related toxicity and improves its antiangiogenic effects, achieving efficacy levels comparable to those of reference compound 2-methoxyestradiol.

Overall, βCPCD emerges as a promising carrier for poorly soluble flavonoids, improving their pharmaceutical and pharmacological performance. Integration early-stage tolerability screening into the formulation development process strengthens this approach's clinical relevance and paves the way for future preclinical studies.

CRediT authorship contribution statement

Federica De Gaetano: Writing – review & editing, Writing – original draft, Visualization, Validation, Methodology, Investigation, Formal analysis, Data curation, Conceptualization. **Eleftheria Dossi:** Writing – review & editing, Supervision, Conceptualization. **Anna Cacciola:** Writing – original draft, Investigation, Data curation. **Noemi Totaro:** Investigation. **Debora Santonocito:** Writing – original draft, Investigation, Data curation. **Luca Pulvirenti:** Investigation. **Salvatore Vincenzo Giofrè:** Writing – original draft, Investigation, Data curation. **Giuseppe Paladini:** Writing – review & editing, Writing – original draft, Visualization, Validation, Methodology, Investigation, Formal analysis, Data curation, Conceptualization. **Alessandro Pilloni:** Writing – review & editing, Validation, Investigation. **Maria Paola Germanò:** Writing – review & editing, Validation, Methodology. **Cinzia Anna Ventura:** Writing – review & editing, Validation, Supervision, Methodology, Formal analysis, Data curation, Conceptualization.

Funding

This work has been partially funded by the European Union (Next-Generation EU) through the MUR-PNRR project SAMOTHRACE (ECS00000022). We also acknowledge the support of the GeV-AI project (CUP I57G21000110007), in the context of the ICSC Spoke 2 Open Calls, project funded by European Union – NextGenerationEU – and National Recovery and Resilience Plan (NRRP) – Mission 4 Component 2.

Declaration of competing interest

The authors declare the following financial interests/personal relationships which may be considered as potential competing interests: [Federica De Gaetano and Cinzia Anna Ventura reports financial support was provided by European Union (NextGeneration EU) through the MUR-PNRR project SAMOTHRACE (ECS00000022). If there are other authors, they declare that they have no known competing financial interests or personal relationships that could have appeared to influence the work reported in this paper].

Appendix A. Supplementary data

Supplementary data to this article can be found online at https://doi.org/10.1016/j.ijpharm.2026.126812.

Data availability

Data will be made available on request.

References

Abraham, M.J., Murtola, T., Schulz, R., Páll, S., Smith, J.C., Hess, B., Lindahl, E., 2015. GROMACS: high performance molecular simulations through multi-level parallelism from laptops to supercomputers. SoftwareX 1–2, 19–25. https://doi.org/10.1016/j.softx.2015.06.001.

Adeoye, O., Conceição, J., Serra, P.A., Bento da Silva, A., Duarte, N., Guedes, R.C., Corvo, M.C., Aguiar-Ricardo, A., Jicsinszky, L., Casimiro, T., Cabral-Marques, H., 2020. Cyclodextrin solubilization and complexation of antiretroviral drug lopinavir: In silico prediction; effects of derivatization, molar ratio and preparation method. Carbohydr. Polym. 227, 115287. https://doi.org/10.1016/j.carbpol.2019.115287.

Al-Dhabi, N.A., Arasu, M.V., Park, C.H., Park, S.U., 2015. An up-to-date review of rutin and its biological and pharmacological activities. EXCLI J. 14, 59. https://doi.org/10.17179/excli2014-663.

Almeleebia, T.M., Goyal, N., Akhter, M.H., Alalmaie, A., Al-Harbi, A.I., Khalilullah, H., Ali, M.S., Alam, M.I., Ahmad, S., Alam, N., Khan, G., Jaremko, M., Emwas, A.-H., 2024. β-cyclodextrin/PVP-stabilized nanocrystal gel for dual release of rutin and thymoquinone for wound healing. J. Clust. Sci. 36, 13. https://doi.org/10.1007/s10876-024-02735-5.

Alonso-Castro, A.J., Domínguez, F., García-Carrancá, A., 2013. Rutin exerts antitumor effects on nude mice bearing SW480 tumor. Arch. Med. Res. 44, 346–351. https://doi.org/10.1016/j.arcmed.2013.06.002.

Al-Ostoot, F.H., Salah, S., Khamees, H.A., Khanum, S.A., 2021. Tumor angiogenesis: current challenges and therapeutic opportunities. Cancer Treatment and Research Communications 28, 100422. https://doi.org/10.1016/j.ctarc.2021.100422.

Alvira, E., 2019. Molecular simulation of the separation of isoleucine enantiomers by β-cyclodextrin. Molecules 24. https://doi.org/10.3390/molecules24061021.

Bansal, K., Bhati, H., Singh, V., Pratap, U., 2025. Advanced nanotechnological approaches for effective delivery of rutin: an updated review. Pharm. Nanotechnol. 13, 916–931. https://doi.org/10.2174/0122117385308249240723111115.

Baumketner, A., 2009. Removing systematic errors in interionic potentials of mean force computed in molecular simulations using reaction-field-based electrostatics. J. Chem. Phys. 130, 104106. https://doi.org/10.1063/1.3081138.

Bazyar, H., Zare Javid, A., Ahangarpour, A., Zaman, F., Hosseini, S.A., Zohoori, V., Aghamohammadi, V., Yazdanfar, S., Ghasemi Deh Cheshmeh, M., 2023. The effects of rutin supplement on blood pressure markers, some serum antioxidant enzymes, and quality of life in patients with type 2 diabetes mellitus compared with placebo. Front. Nutr. 10, 1214420. https://doi.org/10.3389/fnut.2023.1214420.

Berendsen, H.J.C., Postma, J.P.M., van Gunsteren, W.F., Hermans, J., 1981. Interaction models for water in relation to protein hydration. In: Pullman, B. (Ed.), Intermolecular Forces: Proceedings of the Fourteenth Jerusalem Symposium on Quantum Chemistry and Biochemistry Held in Jerusalem, Israel, April 13–16. Springer, Netherlands, Dordrecht, pp. 331–342. https://doi.org/10.1007/978-94-015-7658-1_21.

Bhuvaneswari, S.S., Kumudha, D., 2024. Enhancing the absorption of rutin and effective cancer management through hyaluronic acid functionalized nanoparticles. International Journal of Applied Pharmaceutics 208–217. https://doi.org/10.22159/ijap.2024v16i4.50749.

Bleta, R., Ponchel, A., Monflier, E., 2018. Cyclodextrin-based supramolecular assemblies: a versatile toolbox for the preparation of functional porous materials. Environ. Chem. Lett. 16, 1393–1413. https://doi.org/10.1007/s10311-018-0768-x.

Bussi, G., Donadio, D., Parrinello, M., 2007. Canonical sampling through velocity rescaling. J. Chem. Phys. 126, 014101. https://doi.org/10.1063/1.2408420.

Cacciola, A., D'Angelo, V., De Gaetano, F., Fais, A., Germanò, M.P., Masala, V., Olla, S., Pistarà, V., Stancanelli, R., Tuberoso, C.I.G., Ventura, C.A., 2025. The anti-angiogenic effect of cynara cardunculus l. subsp. cardunculus waste product. Foods 14, 2656. https://doi.org/10.3390/foods14152656.

Calabrò, M.L., Tommasini, S., Donato, P., Stancanelli, R., Raneri, D., Catania, S., Costa, C., Villari, V., Ficarra, P., Ficarra, R., 2005. The rutin/β-cyclodextrin interactions in fully aqueous solution: spectroscopic studies and biological assays. J. Pharm. Biomed. Anal. 36, 1019–1027. https://doi.org/10.1016/j.jpba.2004.09.018.

Cannavà, C., Stancanelli, R., Marabeti, M.R., Venuti, V., Cascio, C., Guarneri, P., Bongiorno, C., Sortino, G., Majolino, D., Mazzaglia, A., Tommasini, S., Ventura, C.A., 2016. Nanospheres based on PLGA/amphiphilic cyclodextrin assemblies as potential enhancers of Methylene Blue neuroprotective effect. RSC Adv. 6, 16720–16729. https://doi.org/10.1039/C5RA27386B.

Chadha, R., Gupta, S., Shukla, G., Jain, D.V.S., Pissurlenkar, R.R.S., Coutinho, E.C., 2011. Interaction of artesunate with β-cyclodextrin: characterization, thermodynamic parameters, molecular modeling, effect of PEG on complexation and antimalarial activity. Results Pharma Sci. 1, 38–48. https://doi.org/10.1016/j.rinphs.2011.07.002.

Chang, C., Song, M., Ma, M., Song, J., Cao, F., Qin, Q., 2023. Preparation, characterization and molecular dynamics simulation of rutin–cyclodextrin inclusion complexes. Molecules 28, 955. https://doi.org/10.3390/molecules28030955.

Chauhan, V., Malviya, N., 2023. Design, development and evaluation of nanosponges loaded topical gel for rejuvenation of skin. International Journal of Drug Delivery Technology 13, 1277–1282. https://doi.org/10.25258/ijddt.13.4.25.

Chen, D., Liu, Y., Liu, P., Zhou, Y., Jiang, L., Yuan, C., Huang, M., 2022. Orally delivered rutin in lipid-based nano-formulation exerts strong antithrombotic effects by protein disulfide isomerase inhibition. Drug Deliv. 29, 1824–1835. https://doi.org/10.1080/10717544.2022.2083726.

Christoforou, I., Kalatzis, A., Siamidi, A., Vlachou, M., Pispas, S., Pippa, N., 2025. The ubiquitous use of polyethylene glycol in pharmaceutical design and development: technological aspects and future perspectives. Nanomaterials 15, 1762. https://doi.org/10.3390/nano15231762.

Concheiro, A., Alvarez-Lorenzo, C., 2013. Chemically cross-linked and grafted cyclodextrin hydrogels: from nanostructures to drug-eluting medical devices. Advanced Drug Delivery Reviews, Polysaccharide-Based Systems in Drug and Gene Delivery 65, 1188–1203. https://doi.org/10.1016/j.addr.2013.04.015.

Conte, P., Delia Francesca Chilllura, M., Paolo, L.M., 2024. Environment in a Magnet: Applications of NMR Techniques to Environmental Problems: [WWW Document]. Environment in a Magnet: Applications of NMR Techniques to Environmental Problems: URL https://www.abebooks.co.uk/9781839167348/Environment-Magnet-Applications-NMR-Techniques-1839167343/plp (accessed 2.26.26).

Corina, D., Florina, B., Iulia, P., Cristina, D., Rita, A., Alexandra, P., Virgil, P., Hancianu, M., Daliana, M., Codruta, S., 2017. Rutin and its cyclodextrin inclusion complexes: physico-chemical evaluation and in vitro activity on B164A5 murine melanoma cell line. Curr. Pharm. Biotechnol. 18, 1067–1077. https://doi.org/10.2174/1389201019666180209165523.

Cristiano, M.C., Barone, A., Mancuso, A., Torella, D., Paolino, D., 2021. Rutin-loaded nanovesicles for improved stability and enhanced topical efficacy of natural compound. Journal of Functional Biomaterials 12, 74. https://doi.org/10.3390/jfb12040074.

da Costa, E.M., Filho, J.M.B., do Nascimento, T.G., Macêdo, R.O., 2002. Thermal characterization of the quercetin and rutin flavonoids. Thermochimica Acta, MATERIAL CHARACTERIZATION BY THERMAL ANALYSIS AND CALORIMETRY. A collection of Papers Scheduled for the 28th North American Thermal Analysis Society Conference Orlando, FL 4-6 October 2000. 392–393, 79–84. 10.1016/S0040-6031(02)00087-4.

De Gaetano, F., Cristiano, M.C., Paolino, D., Celesti, C., Iannazzo, D., Pistarà, V., Iraci, N., Ventura, C.A., 2022. Bicalutamide anticancer activity enhancement by formulation of soluble inclusion complexes with cyclodextrins. Biomolecules 12, 1716. https://doi.org/10.3390/biom12111716.

De Gaetano, F., Cristiano, M.C., Venuti, V., Crupi, V., Majolino, D., Paladini, G., Acri, G., Testagrossa, B., Irrera, A., Paolino, D., Tommasini, S., Ventura, C.A., Stancanelli, R., 2021. Rutin-loaded solid lipid nanoparticles: characterization and in vitro evaluation. Molecules 26, 1039. https://doi.org/10.3390/molecules26041039.

De Gaetano, F., Leggio, L., Celesti, C., Genovese, F., Falcone, M., Giofrè, S.V., Iraci, N., Ventura, C.A., 2024a. Study of host-guest interaction and in vitro neuroprotective potential of cinnamic acid/randomly methylated β-cyclodextrin inclusion complex. Int. J. Mol. Sci. 25, 12778. https://doi.org/10.3390/ijms252312778.

De Gaetano, F., Mannino, D., Celesti, C., Bulzomí, M., Iraci, N., Vincenzo Giofrè, S., Esposito, E., Paterniti, I., Anna Ventura, C., 2024b. Randomly methylated β-cyclodextrin improves water – solubility, cellular protection and mucosa permeability of idebenone. Int. J. Pharm. 665, 124718. https://doi.org/10.1016/j.ijpharm.2024.124718.

De Gaetano, F., Margani, F., Barbera, V., D'Angelo, V., Germanò, M.P., Pistarà, V., Ventura, C.A., 2023. Characterization and in vivo antiangiogenic activity evaluation of morin-based cyclodextrin inclusion complexes. Pharmaceutics 15, 2209. https://doi.org/10.3390/pharmaceutics15092209.

De Gaetano, F., Pastorello, M., Pistarà, V., Rescifina, A., Margani, F., Barbera, V., Ventura, C.A., Marino, A., 2024c. Rutin/sulfobutylether-β-cyclodextrin as a

promising therapeutic formulation for ocular infection. Pharmaceutics 16, 233. https://doi.org/10.3390/pharmaceutics16020233.
De Gaetano, F., Totaro, N., Ventura, C.A., 2025. Cyclodextrin-based formulations as a promising strategy to overcome the blood–brain barrier: historical overview and prospects in glioblastoma treatment. Pharmaceuticals 18, 1626. https://doi.org/10.3390/ph18111626.
El-Remaily, M.A.E.A.A.A., Soliman, A.M.M., 2016. Epichlorohydrin cross-linked β-cyclodextrin: an environmental method for the synthesis of 2-arylbenzothiazoles derivatives in water. J. Sulfur Chem. 37, 70–79. https://doi.org/10.1080/17415993.2015.1089874.
Emmanuel, O.P., Sandrine, M.N.Y., Claude, B.D., Rigobert-Espoir, A.M., Ojo, O.A., Fils, E. A., Ronald, B.A.G., Michel, B.G., Désiré, D.D.P., Aziz, T., Alamri, A.S., Alsanie, W.F., Alhomrani, M., 2025. Anti-breast cancer effects of *Pterocarpus soyauxii* Taub aqueous extract and its compounds by integrating ADMET, network pharmacology, molecular docking, dynamic simulation, CLC-Pred and pdCSM-Cancer/PPI approaches, and *in vitro* validation. J. Ethnopharmacol. 353, 120407. https://doi.org/10.1016/j.jep.2025.120407.
Esteso, M.A., Romero, C.M., 2024. Cyclodextrins: properties and applications. Int. J. Mol. Sci. 25, 4547. https://doi.org/10.3390/ijms25084547.
Feng, J.-F., Tan, M., Zhang, S., Li, B.-J., 2021. Recent advances of porous materials based on cyclodextrin. Macromol. Rapid Commun. 42, 2100497. https://doi.org/10.1002/marc.202100497.
Fenyvesi, F., Klusóczki, Á., Rusznyák, Á., Zsebik, B., Bácskay, I., Váradi, J., 2025. Cyclodextrin-based delivery systems for flavonoids: mechanisms, advances, formulation, and application opportunities. Antioxidants 14, 998. https://doi.org/10.3390/antiox14080998.
Garms, B.C., Poli, H., Baggley, D., Han, F.Y., Whittaker, A.K., A, A., Grøndahl, L., 2021. Evaluating the effect of synthesis, isolation, and characterisation variables on reported particle size and dispersity of drug loaded PLGA nanoparticles. Mater. Adv. 2, 5657–5671. 10.1039/D1MA00410G.
Geue, N., Alcázar, J.J., Campodónico, P.R., 2023. Influence of β-cyclodextrin methylation on host-guest complex stability: a theoretical study of intra- and intermolecular interactions as well as host dimer formation. Molecules 28, 2625. https://doi.org/10.3390/molecules28062625.
Ghorbani, A., 2017. Mechanisms of antidiabetic effects of flavonoid rutin. Biomed. Pharmacother. 96, 305–312. https://doi.org/10.1016/j.biopha.2017.10.001.
Gillespie, C., Kennedy, A.R., Edwards, D., Dowden, L., Daublain, P., Halling, P., 2013. Detailed study of precipitation of a poorly water soluble test compound using methodologies as in activity and solubility screening - mixing and automation effects. Comb. Chem. High Throughput Screen. 16, 636–643. https://doi.org/10.2174/13862073113169990006.
Goyal, N., Amar, A., Gulati, S., Varma, R.S., 2023. Cyclodextrin-based nanosponges as an environmentally sustainable solution for water treatment: a review. ACS Appl. Nano Mater. 6, 13766–13791. https://doi.org/10.1021/acsanm.3c02026.
Gubitosa, J., Cignolo, D., Rizzi, V., Fini, P., Sibillano, T., Corriero, N., Giannini, C., Caldera, F., Desoky, M.M.H., Er-rahmani, S., Trotta, F., Petrella, A., Cosma, P., 2025. Crosslinked α-Cyclodextrin-based metal-organic frameworks: Water-stable adsorbents for enhanced removal of direct textile dyes from aqueous media. 10.1016/j.colsurfa.2025.138312.
Guruvayoorappan, C., Kuttan, G., 2007. Antiangiogenic effect of rutin and its regulatory effect on the production of VEGF, IL-1β and TNF-α in tumor associated macrophages. J. Biol. Sci. 7, 1511–1519. https://doi.org/10.3923/jbs.2007.1511.1519.
Haimhoffer, Á., Dossi, E., Béresová, M., Bácskay, I., Váradi, J., Afsar, A., Rusznyák, Á., Vasvári, G., Fenyvesi, F., 2021. Preformulation studies and bioavailability enhancement of curcumin with a 'two in one' PEG-β-cyclodextrin polymer. Pharmaceutics 13, 1710. https://doi.org/10.3390/pharmaceutics13101710.
Haouas, M., Falaise, C., Leclerc, N., Floquet, S., Cadot, E., 2023. NMR spectroscopy to study cyclodextrin-based host–guest assemblies with polynuclear clusters. Dalton Trans. 52, 13467–13481. https://doi.org/10.1039/D3DT02367B.
Harada, A., Takashima, Y., Yamaguchi, H., 2009. Cyclodextrin-based supramolecular polymers. Chem. Soc. Rev. 38, 875–882. https://doi.org/10.1039/B705458K.
Hassan, A.M., Gattan, H.S., Faizo, A.A., Alruhaili, M.H., Alharbi, A.S., Bajrai, L.H., AL-Zahrani, I.A., Dwivedi, V.D., Azhar, E.I., 2024. Evaluating the binding potential and stability of drug-like compounds with the monkeypox virus VP39 protein using molecular dynamics simulations and free energy analysis. Pharmaceuticals 17. https://doi.org/10.3390/ph17121617.
Hess, B., Bekker, H., Berendsen, H.J.C., Fraaije, J.G.E.M., 1997. LINCS: a linear constraint solver for molecular simulations. J. Comput. Chem. 18, 1463–1472. https://doi.org/10.1002/(SICI)1096-987X(199709)18:12<1463::AID-JCC4>3.0.CO;2-H.
Hou, T., Wang, J., Li, Y., Wang, W., 2011. Assessing the performance of the MM/PBSA and MM/GBSA methods: I. the accuracy of binding free energy calculations based on molecular dynamics simulations. J. Chem. Inf. Model. 51, 69–82. https://doi.org/10.1021/ci100275a.
Hu, Y.-X., Hu, B.-W., Chen, Y.-S., You, H.-M., Bai, M.-R., Zhang, L.-J., Guo, Z.-F., Liang, C., 2023. Di-(2-ethylhexyl) phthalate impairs angiogenesis and hematopoiesis *via* suppressing VEGF signaling in zebrafish. Comp. Biochem. Physiol. C: Toxicol. Pharmacol. 267, 109588. https://doi.org/10.1016/j.cbpc.2023.109588.
Huang, W., Yu, X., Liang, N., Ge, W., Kwok, H.F., Lau, C.-B.-S., Li, Y., Chung, H.Y., 2016. Anti-angiogenic activity and mechanism of sesquiterpene lactones from centipeda minima. Nat. Prod. Commun. 11, 435–438.
Iannuzzi, A.M., Camero, C.M., D'Ambola, M., D'Angelo, V., Amira, S., Bader, A., Braca, A., De Tommasi, N., Germanò, M.P., 2019. Antiangiogenic iridoids from stachys ocymastrum and premna resinosa. Planta Med. 85, 1034–1039. https://doi.org/10.1055/a-0889-0412.
Jiang, T., Zeng, Q., He, J., 2023. Do alkaline phosphatases have great potential in the diagnosis, prognosis, and treatment of tumors? Transl. Cancer Res. 12, 2932–2945. https://doi.org/10.21037/tcr-23-1190.
Jitapunkul, K., Toochinda, P., Lawtrakul, L., 2021. Molecular dynamic simulation analysis on the inclusion complexation of plumbagin with β-cyclodextrin derivatives in aqueous solution. Molecules 26. https://doi.org/10.3390/molecules26226784.
Kali, G., Haddadzadegan, S., Bernkop-Schnürch, A., 2024. Cyclodextrins and derivatives in drug delivery: new developments, relevant clinical trials, and advanced products. Carbohydr. Polym. 324, 121500. https://doi.org/10.1016/j.carbpol.2023.121500.
Kawano, S., Kida, T., Akashi, M., Sato, H., Shizuma, M., Ono, D., 2015. Preparation of Pickering emulsions through interfacial adsorption by soft cyclodextrin nanogels. Beilstein J. Org. Chem. 11, 2355–2364. https://doi.org/10.3762/bjoc.11.257.
Kerbel, R., Folkman, J., 2002. Clinical translation of angiogenesis inhibitors. Nat. Rev. Cancer 2, 727–739. https://doi.org/10.1038/nrc905.
Kicuntod, J., Sangpheak, K., Mueller, M., Wolschann, P., Viernstein, H., Yanaka, S., Kato, K., Chavasiri, W., Pongsawasdi, P., Kungwan, N., Rungrotmongkol, T., 2018. Theoretical and experimental studies on inclusion complexes of pinostrobin and β-cyclodextrins. Sci. Pharm. 86. https://doi.org/10.3390/scipharm86010005.
Kou, X., Su, D., Pan, F., Xu, X., Meng, Q., Ke, Q., 2024. Molecular dynamics simulation techniques and their application to aroma compounds/cyclodextrin inclusion complexes: a review. Carbohydr. Polym. 324, 121524. https://doi.org/10.1016/j.carbpol.2023.121524.
Li, B., Wen, M., Li, W., He, M., Yang, X., Li, S., 2011. Preparation and characterization of baicalin-poly -vinylpyrrolidone coprecipitate. Int. J. Pharm. 408, 91–96. https://doi.org/10.1016/j.ijpharm.2011.01.055.
Li, Z., Liang, S., Sun, H., Bao, C., Li, Y., 2023. Antilipogenesis effect of rutin-loaded liposomes using a microneedle delivery system. ACS Appl. Mater. Interfaces 15, 54294–54303. https://doi.org/10.1021/acsami.3c12795.
Liang, N., Li, Y., Chung, H.Y., 2017. Two natural eudesmane-type sesquiterpenes from Laggera alata inhibit angiogenesis and suppress breast cancer cell migration through VEGF- and Angiopoietin 2-mediated signaling pathways. Int. J. Oncol. 51, 213–222. https://doi.org/10.3892/ijo.2017.4004.
Liang, N., Li, Y.-M., He, Z., Hao, W., Zhao, Y., Liu, J., Zhu, H., Kwek, E., Ma, K.-Y., He, W.-S., Chen, Z.-Y., 2021. Rutin and quercetin decrease cholesterol in HepG2 cells but not plasma cholesterol in hamsters by oral administration. Molecules 26, 3766. https://doi.org/10.3390/molecules26123766.
Liu, B., Li, W., Nguyen, T.A., Zhao, J., 2012. Empirical, thermodynamic and quantum-chemical investigations of inclusion complexation between flavanones and (2-hydroxypropyl)-cyclodextrins. Food Chem. 134, 926–932. https://doi.org/10.1016/j.foodchem.2012.02.207.
Liu, J., Zhang, S., Zhao, X., Lu, Y., Song, M., Wu, S., 2022. Molecular simulation and experimental study on the inclusion of rutin with *β*-cyclodextrin and its derivative. J. Mol. Struct. 1254, 132359. https://doi.org/10.1016/j.molstruc.2022.132359.
Liu, P., Xu, H., Zhang, D., Zhan, J., 2013. Molecular inclusion of PCB126 by beta-cyclodextrin: a combined molecular dynamics simulation and quantum chemical study. J. Incl. Phenom. Macrocycl. Chem. 76, 301–309. https://doi.org/10.1007/s10847-012-0199-4.
Liu, Y., Lin, T., Cheng, C., Wang, Q., Lin, S., Liu, C., Han, X., 2021a. Research progress on synthesis and application of cyclodextrin polymers. Molecules 26, 1090. https://doi.org/10.3390/molecules26041090.
Liu, Y., Zhao, X., Zhang, Q., Wang, L., Li, Y., Li, Y., 2020. Characterization and evaluation of the solubility and oral bioavailability of rutin-ethanolate solvate. AAPS PharmSciTech 21, 241. https://doi.org/10.1208/s12249-020-01779-w.
Liu, Z., Yang, W., Tian, B., Liu, J., Zhu, W., Ge, G., Xiao, L., Meng, Y., 2018. Fabrication of a self-assembled supramolecular fluorescent nanosensor from functional graphene oxide and its application for the detection of Al3+. New J. Chem. 42, 17665–17670. https://doi.org/10.1039/C8NJ03322F.
Liu, Z., Ye, L., Xi, J., Wang, J., Feng, Z., 2021b. Cyclodextrin polymers: Structure, synthesis, and use as drug carriers. Prog. Polym. Sci. 118, 101408. https://doi.org/10.1016/j.progpolymsci.2021.101408.
Loftsson, T., Saokham, P., Sá Couto, A.R., 2019. Self-association of cyclodextrins and cyclodextrin complexes in aqueous solutions. Int. J. Pharm. 560, 228–234. https://doi.org/10.1016/j.ijpharm.2019.02.004.
Luppi, F., Cavaye, H., Dossi, E., 2018. Nitrated cross-linked β-cyclodextrin binders exhibiting low glass transition temperatures. Propellants Explos. Pyrotech. 43, 1023–1031. https://doi.org/10.1002/prep.201800137.
Luppi, F., Kister, G., Carpenter, M., Dossi, E., 2019. Thermomechanical characterisation of cross-linked β-cyclodextrin polyether binders. Polym. Test. 73, 338–345. https://doi.org/10.1016/j.polymertesting.2018.11.034.
Maes, J., Verlooy, L., Buenafe, O.E., de Witte, P.A.M., Esguerra, C.V., Crawford, A.D., 2012. Evaluation of 14 organic solvents and carriers for screening applications in zebrafish embryos and larvae. PLoS One 7, e43850. https://doi.org/10.1371/journal.pone.0043850.
Mahalapbutr, P., Wonganan, P., Charoenwongpaiboon, T., Prousoontorn, M., Chavasiri, W., Rungrotmongkol, T., 2019. Enhanced solubility and anticancer potential of mansonone G by β-cyclodextrin-based host-guest complexation: a computational and experimental study. Biomolecules 9. https://doi.org/10.3390/biom9100545.
Malekpour, M., Ebrahiminezhad, A., Karimi, Z., Saadi, M.I., Berenjian, A., 2025. Current strategies for rutin nano-formulation; a promising bioactive compound with increased efficacy. Bioprocess Biosyst. Eng. 48, 877–898. https://doi.org/10.1007/s00449-025-03156-y.
Mallard, I., Landy, D., Fourmentin, S., 2020. Evaluation of polyethylene glycol crosslinked β-CD polymers for the removal of methylene blue. Appl. Sci. 10, 4679. https://doi.org/10.3390/app10134679.

Matteini, P., Goti, A., Agati, G., 2010. Theoretical conformational analysis of rutin. Monatsh. Chem. 141, 793–800. https://doi.org/10.1007/s00706-010-0330-4.
Minea, B., Marangoci, N., Peptanariu, D., Rosca, I., Nastasa, V., Corciova, A., Varganici, C., Nicolescu, A., Fifere, A., Neamtu, A., Mares, M., Barboiu, M., Pinteala, M., 2016. Inclusion complexes of propiconazole nitrate with substituted β-cyclodextrins: the synthesis and in silico and in vitro assessment of their antifungal properties. New J. Chem. 40, 1765–1776. https://doi.org/10.1039/C5NJ01811K.
Ming Liu, W., Yun Zhou, H., Qiang Jiang, S., Ping Dai, S., Wang, Y., Jia Yang, J., Wei Chen, Y., Liang Chen, J., Jin Park, H., 2024. Inclusion complexation of flavonoids with cyclodextrin: molecular docking and experimental study. ChemistrySelect 9, e202403606. https://doi.org/10.1002/slct.202403606.
Mojdehi, M.F.P., Koli, M.G., Bolagh, M.D.O., Gardeh, M.G., Majid Hashemianzadeh, S., 2021. A detailed computational study on binding of kinase inhibitors into β-cyclodextrin: inclusion complex formation. Mol. Syst. Des. Eng. 6, 80–92. https://doi.org/10.1039/D0ME00140F.
Mooberry, S.L., 2003. New insights into 2-methoxyestradiol, a promising antiangiogenic and antitumor agent. Curr. Opin. Oncol. 15, 425–430. https://doi.org/10.1097/00001622-200311000-00004.
Morin-Crini, N., Winterton, P., Fourmentin, S., Wilson, L.D., Fenyvesi, É., Crini, G., 2018. Water-insoluble β-cyclodextrin–epichlorohydrin polymers for removal of pollutants from aqueous solutions by sorption processes using batch studies: a review of inclusion mechanisms. Prog. Polym. Sci. 78, 1–23. https://doi.org/10.1016/j.progpolymsci.2017.07.004.
Mourad, R., El Mogy, S.A., Darwesh, O., Abdel-Hakim, A., 2024. In-vitro evaluation of antimicrobial and anti-inflammatory efficacy of the gelatin-β-cyclodextrin hydrogels as biodegradable carriers for rutin. ChemistrySelect 9, e202303705. https://doi.org/10.1002/slct.202303705.
Muankaew, C., Saokham, P., Jansook, P., Loftsson, T., 2020. Self-assembly of cyclodextrin complexes: detection, obstacles and benefits. Pharmazie 75, 307–312. https://doi.org/10.1691/ph.2020.0405.
Muthukkaruppan, V.R., Kubai, L., Auerbach, R., 1982. Tumor-induced neovascularization in the mouse eye. J. Natl Cancer Inst. 69, 699–708.
Naeem, A., Yu, C., Zang, Z., Zhu, W., Deng, X., Guan, Y., 2023. Synthesis and evaluation of rutin–hydroxypropyl β-cyclodextrin inclusion complexes embedded in xanthan gum-based (HPMC-g-AMPS) hydrogels for oral controlled drug delivery. Antioxidants 12. https://doi.org/10.3390/antiox12030552.
Najmi, A., Javed, S.A., Al Bratty, M., Alhazmi, H.A., 2022. Modern approaches in the discovery and development of plant-based natural products and their analogues as potential therapeutic agents. Molecules 27, 349. https://doi.org/10.3390/molecules27020349.
Narayanankutty, A., Famurewa, A.C., Oprea, E., 2024. Natural bioactive compounds and human health. Molecules 29, 3372. https://doi.org/10.3390/molecules29143372.
Naveed, M., Ali, A., Aziz, T., Ali, N., Rehman, H.M., Khan, A.A., ul Haq, T., El Hadi Mohamed, R.A., Al-Asmari, F., Alwethaynani, M.S., Al-Joufi, F.A., Fallatah, D., 2025. Computational design of a glycosylated multi-epitope vaccine against HAsV-1 and HAsV-2 astrovirus for acute gastroenteritis. Sci. Rep. 15, 13954. https://doi.org/10.1038/s41598-025-96989-2.
Naveed, M., Asim, M., Aziz, T., Ibrahim, S., Aqeel, Z.B., Majeed, M.N., Hussain, N., Mohamed, R.A.E.H., Al-Joufi, F.A., Alwethaynani, M.S., 2026. Designing IL-24-P18 fusion protein through computational engineering for targeted breast cancer therapy. J. Comput. Biophys. Chem. 25, 109–123. https://doi.org/10.1142/S2737416525500383.
Nguyen, H.V., Nguyen, N.-T.-T., Tran, H.-K.-T., Huynh, T.-T.-N., Vo, V.-H.-B., Le, C.-T.-T., Saha, T., 2025. Improved dissolution of poorly water-soluble rutin via solid dispersion prepared using a fluid-bed coating system. Pharmaceutics 17, 1559. https://doi.org/10.3390/pharmaceutics17121559.
Nguyen, T.A., Liu, B., Zhao, J., Thomas, D.S., Hook, J.M., 2013. An investigation into the supramolecular structure, solubility, stability and antioxidant activity of rutin/cyclodextrin inclusion complex. Food Chem. 136, 186–192. https://doi.org/10.1016/j.foodchem.2012.07.104.
Nishida, N., Yano, H., Nishida, T., Kamura, T., Kojiro, M., 2006. Angiogenesis in cancer. Vasc. Health Risk Manag. 2, 213–219.
Oostenbrink, C., Villa, A., Mark, A.E., Van Gunsteren, W.F., 2004. A biomolecular force field based on the free enthalpy of hydration and solvation: the GROMOS force-field parameter sets 53A5 and 53A6. J. Comput. Chem. 25, 1656–1676. https://doi.org/10.1002/jcc.20090.
Paladini, G., De Gaetano, F., Venuti, V., Caridi, F., Faggio, G., Messina, G., Lombardo, C., Majolino, D., Mottese, A.F., Pistarà, V., Pistorino, L., Salmeri, M., Stancanelli, R., Tommasini, S., Ventura, C.A., 2025. Development, physicochemical characterization and antibacterial evaluation of the baicalin/sulfobutylether-β-cyclodextrin inclusion complex. Int. J. Pharm. 684, 126178. https://doi.org/10.1016/j.ijpharm.2025.126178.
Pandey, P., Khan, F., Qari, H.A., Oves, M., 2021. Rutin (Bioflavonoid) as cell signaling pathway modulator: prospects in treatment and chemoprevention. Pharmaceuticals (Basel) 14, 1069. https://doi.org/10.3390/ph14111069.
Papetti, M., Herman, I.M., 2002. Mechanisms of normal and tumor-derived angiogenesis. Am. J. Physiol. Cell Physiol. 282, C947–C970. https://doi.org/10.1152/ajpcell.00389.2001.
Pedotti, S., Pistarà, V., Cannavà, C., Carbone, C., Cilurzo, F., Corsaro, A., Puglisi, G., Ventura, C.A., 2015. Synthesis and physico-chemical characterization of a β-cyclodextrin conjugate for sustained release of Acyclovir. Carbohydr. Polym. 131, 159–167. https://doi.org/10.1016/j.carbpol.2015.05.071.
Pham, T.L., Nguyen, T.T.H., Nguyen, T.A., Le-Deygen, I., Le, T.M.H., Vu, X.M., Le, H.K., Van, C.B., Usacheva, T.R., Mai, T.T., Tran, D.L., 2024. Antioxidant activity of an inclusion complex between rutin and β-cyclodextrin: experimental and quantum chemical studies. RSC Adv. 14, 18330–18342. https://doi.org/10.1039/D4RA02307B.
Picco, A.S., Mondo, G.B., Ferreira, L.F., de Souza, E.E., Peroni, L.A., Cardoso, M.B., 2021. Protein corona meets freeze-drying: overcoming the challenges of colloidal stability, toxicity, and opsonin adsorption. Nanoscale 13, 753–762. https://doi.org/10.1039/D0NR06040B.
Poger, D., Mark, A.E., 2010. On the validation of molecular dynamics simulations of saturated and cis-monounsaturated phosphatidylcholine lipid bilayers: a comparison with experiment. J. Chem. Theory Comput. 6, 325–336. https://doi.org/10.1021/ct900487a.
Poger, D., Van Gunsteren, W.F., Mark, A.E., 2010. A new force field for simulating phosphatidylcholine bilayers. J. Comput. Chem. 31, 1117–1125. https://doi.org/10.1002/jcc.21396.
Poonphatanapricha, T., Katanyutanon, S., Jitapunkul, K., Lawtrakul, L., Toochinda, P., 2021. The preservation and enantiomeric selection of linalool by nanoencapsulation using cyclodextrins. Sci. Pharm. 89. https://doi.org/10.3390/scipharm89030042.
Popa-Burke, I., Russell, J., 2014. Compound precipitation in high-concentration DMSO solutions. J. Biomol. Screen. 19, 1302–1308. https://doi.org/10.1177/1087057114541146.
Pravin, B., Nanaware, V., Ashwini, B., Wondmie, G.F., Jardan, Y.A.B., Bourhia, M., 2024. Assessing the antioxidant properties of Naringin and Rutin and investigating their oxidative DNA damage effects in breast cancer. Sci. Rep. 14, 15314. https://doi.org/10.1038/s41598-024-63498-7.
Puig-Rigall, J., Serra-Gómez, R., Stead, I., Grillo, I., Dreiss, C.A., González-Gaitano, G., 2019. Pseudo-polyrotaxanes of cyclodextrins with direct and reverse x-shaped block copolymers: a kinetic and structural study. Macromolecules 52, 1458–1468. https://doi.org/10.1021/acs.macromol.8b02509.
Raina, N., Singh, A.K., Islam, A., 2021. Biological implications of polyethylene glycol and pegylation: therapeutic approaches based on biophysical studies and protein structure-based drug design tools. In: Singh, S.K. (Ed.), Innovations and Implementations of Computer Aided Drug Discovery Strategies in Rational Drug Design, pp. 273–294. https://doi.org/10.1007/978-981-15-8936-2_11.
Rashidinejad, A., Dima, C., Can Karaca, A., Jafari, S.M., 2024. A review on rutin-loaded nanocarriers: fundamentals, bioavailability, application in functional foods, and challenges. Eur. Polym. J. 219, 113385. https://doi.org/10.1016/j.eurpolymj.2024.113385.
Rodriguez-Tenreiro, C., Alvarez-Lorenzo, C., Rodriguez-Perez, A., Concheiro, A., Torres-Labandeira, J.J., 2006. New cyclodextrin hydrogels cross-linked with diglycidylethers with a high drug loading and controlled release ability. Pharm. Res. 23, 121–130. https://doi.org/10.1007/s11095-005-8924-y.
Rojas-Aguirre, Y., Torres-Mena, M.A., López-Méndez, L.J., Alcaraz-Estrada, S.L., Guadarrama, P., Urucha-Ortíz, J.M., 2019. PEGylated β-cyclodextrins: click synthesis and in vitro biological insights. Carbohydr. Polym. 223, 115113. https://doi.org/10.1016/j.carbpol.2019.115113.
Ryzhakov, A., Do Thi, T., Stappaerts, J., Bertoletti, L., Kimpe, K., Sá Couto, A.R., Saokham, P., Van den Mooter, G., Augustijns, P., Somsen, G.W., Kurkov, S., Inghelbrecht, S., Arien, A., Jimidar, M.I., Schrijnemakers, K., Loftsson, T., 2016. Self-assembly of cyclodextrins and their complexes in aqueous solutions. J. Pharm. Sci. 105, 2556–2569. https://doi.org/10.1016/j.xphs.2016.01.019.
Sadia, H., Qureshi, I.Z., Naveed, M., Aziz, T., Alharbi, M., Alasmari, A.F., Albekairi, T.H., 2024. Natural AI-based drug designing by modification of ascorbic acid and curcumin to combat buprofezin toxicity by using molecular dynamics study. Sci. Rep. 14, 28445. https://doi.org/10.1038/s41598-024-79275-5.
Sajeesh, S., Sharma, C.P., 2006. Cyclodextrin-insulin complex encapsulated polymethacrylic acid based nanoparticles for oral insulin delivery. Int. J. Pharm. 325, 147–154. https://doi.org/10.1016/j.ijpharm.2006.06.019.
Saokham, P., Muankaew, C., Jansook, P., Loftsson, T., 2018. Solubility of cyclodextrins and drug/cyclodextrin complexes. Molecules 23, 1161. https://doi.org/10.3390/molecules23051161.
Savic, I.M., Savic-Gajic, I.M., Nikolic, V.D., Nikolic, L.B., Radovanovic, B.C., Milenkovic-Andjelkovic, A., 2016. Enhencemnet of solubility and photostability of rutin by complexation with β-cyclodextrin and (2-hydroxypropyl)-β-cyclodextrin. J. Incl. Phenom. Macrocycl. Chem. 86, 33–43. https://doi.org/10.1007/s10847-016-0638-8.
Schmid, N., Eichenberger, A.P., Choutko, A., Riniker, S., Winger, M., Mark, A.E., van Gunsteren, W.F., 2011. Definition and testing of the GROMOS force-field versions 54A7 and 54B7. Eur. Biophys. J. 40, 843–856. https://doi.org/10.1007/s00249-011-0700-9.
Serri, C., Quagliariello, V., Cruz-Maya, I., Guarino, V., Maurea, N., Giunchedi, P., Rassu, G., Gavini, E., 2024. Hyaluronic acid-based nanoparticles loaded with rutin as vasculo-protective tools against anthracycline-induced endothelial damages. Pharmaceutics 16, 985. https://doi.org/10.3390/pharmaceutics16080985.
Sguizzato, M., Ferrara, F., Sisto, M., Drechsler, M., Gallerani, E., Nicoli, F., Cortesi, R., 2025. Rutin-containing cyclodextrin nanosystems: a possible strategy for dietary supplementation in diabetics. J. Drug Delivery Sci. Technol. 110, 107065. https://doi.org/10.1016/j.jddst.2025.107065.
Sharma, S., Ali, A., Ali, J., Sahni, J.K., Baboota, S., 2013a. Rutin: therapeutic potential and recent advances in drug delivery. Expert Opin. Invest. Drugs 22, 1063–1079. https://doi.org/10.1517/13543784.2013.805744.
Sharma, S., Ali, A., Ali, J., Sahni, J.K., Baboota, S., 2013b. Rutin: therapeutic potential and recent advances in drug delivery. Expert Opin. Invest. Drugs 22, 1063–1079. https://doi.org/10.1517/13543784.2013.805744.
Shurshina, A., Bazunova, M., Chernova, V., Galina, A., Titlova, A., Kulish, E., 2021. The impact of polymers' supramolecular structure on water vapour sorption and drug release from films on the basis of some polysaccharide. J. Drug Delivery Sci. Technol. 63, 102560. https://doi.org/10.1016/j.jddst.2021.102560.

Sirin, M., Zeybek, M.S., Sirin, K., Abali, Y., 2022. Effect of gamma irradiation on the thermal and mechanical behaviour of polypropylene and polyethylene blends. Radiat. Phys. Chem. 194, 110034. https://doi.org/10.1016/j.radphyschem.2022.110034.

Sri, K.V., Santhoshini, G., Sankar, D.R., Niharika, K., 2018. Formulation and evaluation of rutin loaded nanosponges. Asian Journal of Research in Pharmaceutical Science 8, 21–24.

Stancanelli, R., Løjkner, L.D., Larsen, K.L., Guardo, M., Cannavà, C., Tommasini, S., Ventura, C.A., Calabrò, M.L., Micali, N., Villari, V., Mazzaglia, A., 2012. Structural and spectroscopic features of lutein/butanoyl-β-cyclodextrin nanoassemblies. J. Pharm. Biomed. Anal. 71, 214–218. https://doi.org/10.1016/j.jpba.2012.07.034.

Stroet, M., Caron, B., Visscher, K.M., Geerke, D.P., Malde, A.K., Mark, A.E., 2018. Automated topology builder version 3.0: prediction of solvation free enthalpies in water and hexane. J. Chem. Theory Comput. 14, 5834–5845. https://doi.org/10.1021/acs.jctc.8b00768.

Suleman, M., Khan, T.A., Ejaz, H., Maroof, S., Alshammari, A., Albekairi, N.A., Khan, H., Waheed, Y., Khan, A., Wei, D.-Q., Crovella, S., 2024. Structural vaccinology, molecular simulation and immune simulation approaches to design multi-epitopes vaccine against John Cunningham virus. Microb. Pathog. 189, 106572. https://doi.org/10.1016/j.micpath.2024.106572.

Swaminathan, S., Cavalli, R., Trotta, F., 2016. Cyclodextrin-based nanosponges: a versatile platform for cancer nanotherapeutics development. WIREs Nanomed. Nanobiotechnol. 8, 579–601. https://doi.org/10.1002/wnan.1384.

Tejashri, G., Amrita, B., Darshana, J., 2013. Cyclodextrin based nanosponges for pharmaceutical use: a review. Acta Pharm. 63, 335–358. https://doi.org/10.2478/acph-2013-0021.

Trotta, F., Shende, P., Biasizzo, M., 2012a. Method for preparing dextrin nanosponges. WO2012147069A1.

Trotta, F., Zanetti, M., Cavalli, R., 2012. Cyclodextrin-based nanosponges as drug carriers. Beilstein J. Org. Chem. 8, 2091–2099. https://doi.org/10.3762/bjoc.8.235.

Tsai, Y.-C., Chiu, C.-C., 2022. Solute diffusivity and local free volume in cross-linked polymer network: implication of optimizing the conductivity of polymer electrolyte. Polymers 14, 2061. https://doi.org/10.3390/polym14102061.

Utzeri, G., Matias, P.M.C., Murtinho, D., Valente, A.J.M., 2022. Cyclodextrin-based nanosponges: overview and opportunities. Front. Chem. 10. https://doi.org/10.3389/fchem.2022.859406.

van de Manakker, F., Vermonden, T., van Nostrum, C.F., Hennink, W.E., 2009. Cyclodextrin-based polymeric materials: synthesis, properties, and pharmaceutical/biomedical applications. Biomacromolecules 10, 3157–3175. https://doi.org/10.1021/bm901065f.

Venuti, V., Crupi, V., Fazio, B., Majolino, D., Acri, G., Testagrossa, B., Stancanelli, R., De Gaetano, F., Gagliardi, A., Paolino, D., Floresta, G., Pistarà, V., Rescifina, A., Ventura, C.A., 2019. Physicochemical characterization and antioxidant activity evaluation of idebenone/hydroxypropyl-β-cyclodextrin inclusion complex †. Biomolecules 9, 531. https://doi.org/10.3390/biom9100531.

Venuti, V., Stancanelli, R., Acri, G., Crupi, V., Paladini, G., Testagrossa, B., Tommasini, S., Ventura, C.A., Majolino, D., 2017. "Host-guest" interactions in Captisol®/Coumestrol inclusion complex: UV–vis, FTIR-ATR and Raman studies. J. Mol. Struct. 1146, 512–521. https://doi.org/10.1016/j.molstruc.2017.06.054.

Wang, J., Guo, Z., Xiong, J., Wu, D., Li, S., Tao, Y., Qin, Y., Kong, Y., 2019. Facile synthesis of chitosan-grafted beta-cyclodextrin for stimuli-responsive drug delivery. Int. J. Biol. Macromol. 125, 941–947. https://doi.org/10.1016/j.ijbiomac.2018.12.150.

Wang, Z., Zheng, L., Yang, S., Niu, R., Chu, E., Lin, X., 2007. N-acetylchitooligosaccharide is a potent angiogenic inhibitor both in vivo and in vitro. Biochem. Biophys. Res. Commun. 357, 26–31. https://doi.org/10.1016/j.bbrc.2007.03.094.

Waybright, T.J., Britt, J.R., McCloud, T.G., 2009. Overcoming problems of compound storage in DMSO: solvent and process alternatives. J. Biomol. Screen. 14, 708–715. https://doi.org/10.1177/1087057109335670.

Wehl, L., Muggli, K., Möller, K., Engelke, H., Bein, T., 2025. Cross-linked cyclodextrin-based nanoparticles as drug delivery vehicles: synthesis strategy and degradation studies. ACS Omega 10, 10352–10365. https://doi.org/10.1021/acsomega.4c10200.

Weiss-Errico, M.J., Berry, J.P., O'Shea, K.E., 2017. β-cyclodextrin attenuates perfluorooctanoic acid toxicity in the zebrafish embryo model. Toxics 5, 31. https://doi.org/10.3390/toxics5040031.

Westerfield, M., 2000. The zebrafish book: a guide for the laboratory use of zebrafish (danio rerio). University of Oregon Press.

Xie, A., Zhang, M., Inoue, S.-I., 2016. Influence of diisocyanate on polyurethane elastomers which crosslinked by β-cyclodextrin. Open Journal of Organic Polymer Materials 6, 99–111. https://doi.org/10.4236/ojopm.2016.63010.

Zhang, H., Ge, C., van der Spoel, D., Feng, W., Tan, T., 2012. Insight into the structural deformations of beta-cyclodextrin caused by alcohol cosolvents and guest molecules. J. Phys. Chem. B 116, 3880–3889. https://doi.org/10.1021/jp300674d.

Zhao, L., Tang, B., Tang, P., Sun, Q., Suo, Z., Zhang, M., Gan, N., Yang, H., Li, H., 2020. Chitosan/sulfobutylether-β-cyclodextrin nanoparticles for ibrutinib delivery: a potential nanoformulation of novel kinase inhibitor. J. Pharm. Sci. 109, 1136–1144. https://doi.org/10.1016/j.xphs.2019.10.007.

Zheng, X., Zhang, X., Zeng, F., 2025. Biological functions and health benefits of flavonoids in fruits and vegetables: a contemporary review. Foods 14, 155. https://doi.org/10.3390/foods14020155.

Zhou, C.J., Li, L.F., Liu, Y., Wen, S.P., Guo, Y.E., Niu, X.G., 2012. Study on the inclusion complex of rutin/sulfobutylether-β-cyclodextrin. Adv. Mat. Res. 455–456, 1177–1181. https://doi.org/10.4028/www.scientific.net/AMR.455-456.1177.

Ziaee, A., Zamansoltani, F., Nassiri-Asl, M., Abbasi, E., 2009. Effects of rutin on lipid profile in hypercholesterolaemic rats. Basic Clin. Pharmacol. Toxicol. 104, 253–258. https://doi.org/10.1111/j.1742-7843.2008.00368.x.

Zvezdanovic, J., Stanojevic, J., Markovic, D., Cvetkovic, D., 2012. Irreversible UV-induced quercetin and rutin degradation in solution, studied by UV-spectrophotometry and HPLC chromatography. J. Serb. Chem. Soc. 77, 297–312. https://doi.org/10.2298/JSC110618180Z.



https://dspace.org/

PEG--Cyclodextrin polymer-based formulation to increase the antiangiogenic activity of rutin in vivo

Gaetano, Federica De; Dossi, Eleftheria; Cacciola, Anna; Totaro, Noemi; Santonocito, Debora ...

2026-05-05
Elsevier
https://doi.org/10.1016/j.ijpharm.2026.126812
Gaetano FD, Dossi E, Cacciola A, et al., (2026) PEG--Cyclodextrin polymer-based formulation to increase the antiangiogenic activity of rutin in vivo. International Journal of Pharmaceutics, Volume 696, May 2026, Article number 126812

Downloaded from a DSpace repository. https://dspace.org/